Mineralogia, vol. 53, 2022, 82-108 *Original Paper*

DOI: 10.2478/mipo-2022-0007

Early Devonian sinistral shearing recorded by retrograde monazite-(Ce) in Oscar II Land, Svalbard

Grzegorz Ziemniak[1,2]*
Maciej Manecki[2]
Pauline Jeanneret[3]
Katarzyna Walczak[2]
Karolina Kośmińska[2]

[1]Institute of Geological Sciences, University of Wrocław, Pl. M. Borna 9, 50-204 Wrocław, Poland
[2]AGH University of Science and Technology, Faculty of Geology, Geophysics and Environmental Protection, al. Mickiewicza 30, 30-059 Kraków, Poland
[3]Uppsala University, Department of Earth Sciences, Villavägen 16, 752 36 Uppsala, Sweden
*Corresponding author: e-mail: grzegorz.ziemniak@uwr.edu.pl

Abstract

The Southwestern Basement Province of Svalbard extends northward from Sørkapp Land in the south to Oscar II Land. In the north, the Müllerneset Formation characterized by polymetamorphosed Proterozoic sedimentary rocks crops out. In this study we used an integrated tectonic and petrochronological approach to gain an insight into the structural and metamorphic evolution of the unit and surrounding basement. The Müllerneset Formation consists of two separate tectonic blocks. NNW-SSE trending retrograde foliation is associated with mineral and stretching lineation and kinematic indicators consistent with left-lateral to oblique sinistral shearing in the western block. The eastern block is characterized by the opposite sense of shear that was overturned during the Eurekan event as evidenced by unconformably overlaying Carboniferous sedimentary rocks. Conventional geothermobarometry yields the prograde peak pressure metamorphic conditions of 6.6 - 7.1 kbar at 480 - 520°C followed by peak temperature at 5.1 - 5.9 kbar and 530 - 560°C. Subsequent retrograde greenschist facies overprint is related to left-lateral NNW-SSE trending shearing. Tiny monazite occurs within foliation or overgrows allanite-(Ce), thus is interpreted as growth along a retrograde path. Th-U-total Pb dating of monazite-(Ce) provided an early Caledonian age (ca. 450 Ma) and younger population of ca. 410 ± 8 Ma. This age is consistent with previously reported $^{40}Ar/^{39}Ar$ cooling ages (410 ± 2 Ma) of muscovite supporting a retrograde growth of monazite. Petrochronological evidence combined with structural observations suggests that the Müllerneset Formation has been tectonically exhumed in the Early Devonian due to the NNW-SSE trending left-lateral shearing. Coeval folding and thrusting in the remaining basement of Oscar II Land to the east indicate

a transpressional regime of the deformation in the Early Devonian. Similarly oriented contemporaneous tectonic zones within the Southwestern Basement Province of Svalbard may account for the same set of shear zones dispersing the Ordovician subduction complexes along western Spitsbergen.

Keywords: Retrograde monazite-(Ce), Svalbard's Southwestern Basement Province, U-Th-total Pb geochronology, Müllerneset Formation, Caledonian Orogeny

1. Introduction

The North Atlantic Caledonides result from nearly orthogonal collision between Laurentia and Baltica in the Silurian and Devonian, when continental margins and remnants of the Iapetus Ocean were transported onto both paleocontinents forming tens of kilometres thick nappe stacks (e.g. Gee 1975; Gee et al. 2008; Higgins 1976). The northernmost section of the Caledonian orogen was dominated by transpression and the displacements along NE-SW-trending strike-slip faulting continued from the late Silurian until the Late Devonian (Hallett et al. 2014; Ohta 1994). Lateral shear zones have been documented or inferred at the boundaries of and within the Pearya Terrane of northern Ellesmere Island (McClelland et al. 2012; von Gosen et al. 2012), north-east Greenland (Hallet et al. 2014; Holdsworth, Strachan 1991), Svalbard Basement Provinces (Faehnrich et al. 2020; Gasser, Andresen 2013; Gee, Teben'kov 2004; Harland, Wrigth 1979; Liberis, Manby 1999; Majka et al. 2015; Mazur et al. 2009). Some of these shear zones might be connected to Caledonian transcurrent faults (NE Greenland, Svalbard), while others are most likely kinematically linked to Late Ordovician – Devonian fault system along northern Laurentian margin (the Canadian Arctic Transform System – CATS; McClelland et al. 2021). The Southwestern Basement Province of Svalbard (SBP) is a particularly interesting target to study the transition of the Caledonian Orogeny from orthogonal to transpressional and its interaction with the CATS. It contains both high-pressure (HP) metamorphic complexes characteristic for the Baltican margin (e.g. Barnes et al. 2020; Elvevold et al. 2014; Hirajima et al. 1988; Labrousse et al. 2008;) and the record of the transpressional late-Caledonian or CATS related faulting (e.g. Faehnrich et al. 2020; Mazur et al. 2009). Additionally, its complex internal structure with several subprovinces or terranes (e.g. Harland 1997; Wala et al. 2021) allows the assessment of the relative movements of the crustal fragments comprising the northern extent of Caledonian Orogen.

Monazite is a mineral commonly used for dating emplacement of the felsic intrusions (Finger et al. 2003) as well as a wide range of metamorphic processes (e.g. Engi et al. 2017). The growth of monazite in high-grade metamorphic rocks is frequently associated with its precipitation from melt both along the prograde and retrograde path (e.g. Kelsey et al. 2008).

In the subsolidus field monazite can grow in pelitic rocks that undergo metamorphism in amphibolite facies conditions when it often forms in prograde reaction in the expense of allanite (e.g. Janots et al. 2006). However, monazite can also grow in the greenschist facies conditions during the retrogressive breakdown of allanite, providing useful insights about the timing of the exhumation of metapelitic rocks (e.g. Palin et al. 2015). Monazite formed in the low-grade stages of the retrograde path is considered troublesome as it can obscure information provided by its prograde generation due to partial resetting (e.g. Seydoux-Guillaume et al. 2018) as well as its tendency to Pb-inheritance, which generates falsely old model dates (e.g. Barnes et al. 2020). Nevertheless, a proper petrochronological approach can allow us to use the geochronological potential of retrograde monazite, when no earlier generations of monazite are present. Th-U-total Pb dating can allow to analyse small (>10 μm) or irregular blasts and can provide a reliable timing of retrogressive metamorphism. Thus, monazite can provide an alternative or be complimentary to other low-temperature geochronometers.

Hereby we present new evidence for a late Silurian – Early Devonian sinistral strike-slip zone dividing the SBP. For the first time, Early Devonian timing of shearing within the SBP is constrained using Th-U-total Pb dating of monazite. Rarely observed retrogressive growth of metamorphic monazite (e.g. Palin et al. 2015; Pan 1997) offers a unique opportunity for dating middle crustal level shear zones. A resemblance of the tectonic scenario documented in this paper with the accretionary structures observed in the Pearya Terrane (e.g. Trettin 1998) supports connection between SBP and the Pearya Terrane in Early Devonian (e.g. Barnes et al. 2020; Gee,

Teben'kov 2004; Majka et al. 2015; Mazur et al. 2009; Trettin 1987).

2. Geological Background

Inhomogeneity of the Svalbard basement related to differences in stratigraphy and tectonothermal evolution of pre-Devonian basement units inspired several terrane models (e.g. Harland, Gayer 1972; Gee, Page 1994; Gee, Teben'kov 2004). The commonly accepted tripartite division of the Svalbard pre-Devonian basement consists of the Eastern, Northwestern and Southwestern Basement Provinces (e.g. Gee 1986; Gee, Page 1994; Gee, Teben'kov 2004; Fig. 1a). The provinces themselves have a composite structure and several internal tectonic boundaries that separate crustal blocks with a dissimilar geological record (e.g. Bazarnik et al. 2019; Gasser, Andersen 2013; Gee, Teben'kov 2004; Mazur et al. 2009; Wala et al. 2021). The Eastern Basement Province (EBP) and the Northwestern Basement Province (NBP) are separated by the Billefjorden Fault zone - the N-S trending transcurrent sinistral strike-slip zone dated to ca. 450 Ma via $^{40}Ar/^{39}Ar$ on muscovite (Gee, Teben'kov 2004; Harland 1972; Harland, Wright 1979; Michalski et al. 2012). Both provinces are correlated with the North-East Greenland Caledonides, based on common igneous histories, Proterozoic sedimentary record and the Caledonian tectonometamorphic evolution characterized by migmatization, westward thrusting and post-orogenic granites emplacement (e.g. Bazarnik et al. 2019; Gee, Teben'kov 2004). The late-Caledonian transpressional events are poorly characterized in the EBP, where only a single ca. 410 Ma U-Pb titanite age is interpreted as the timing of a kinematically undefined shearing event (Harland 1972; Johansson et al. 1995; Lyberis, Manby 1999). In the NBP two episodes of late-Silurian-early Devonian deformation recorded at ca. 420-410 Ma post-date the ca. 423 Ma amphibolite facies metamorphism in the Biscayarhalvøya Terrane and deposition of the late Silurian-Early Devonian(?) Siktefjellet Group (e.g. Koglin et al. 2022; McCann 2000). The earlier activity of the dextral NNW-SSE trending Biscayarhalvøya Shear Zone and Lerner Deformation Zone was dated via U-Pb geochronology of zircon in syntectonic granites to ca. 421 – 415 Ma (Koglin et al. 2022; McCann 2000; Piepjohn, Thiedig 1995). This late Silurian deformation is also expressed as the unconformity pre-dating the Lokhovian Red Bay Group sediments and tilting of the Siktefjellet Group resulting from sinistral shearing along the Breibogen-Bockfjorden and Rabotdalen-Hannabreen fault zones (Friend et al. 1997; McCann 2000). The following phase of presumably Pragian age was related to the sinistral strike-slip along the NNW-SSE trending Raudfjorden Fault accompanied by minor shortening with local eastward vergence of tectonic transport (McCann 2000). However, the timing of this phase is constrained

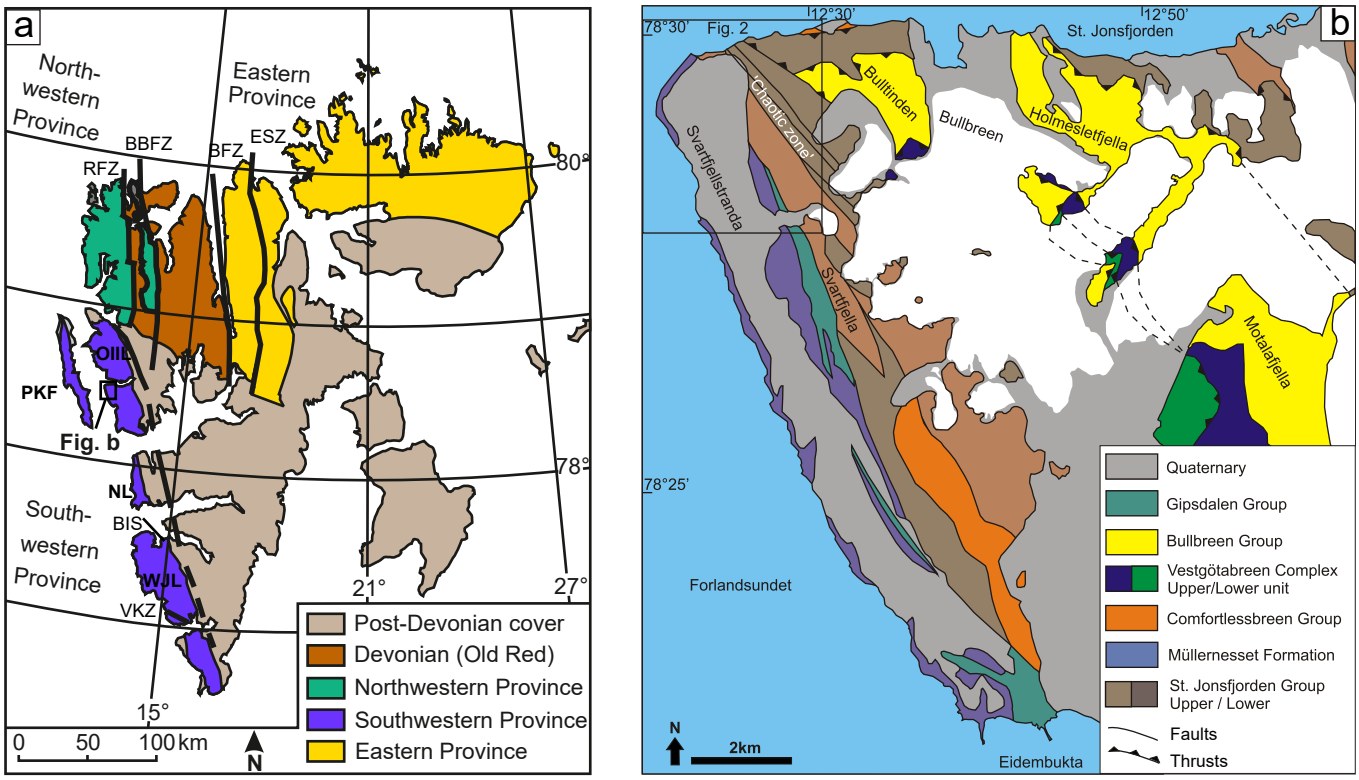

Figure 1. (a) Geological map of Svalbard (modified from Gee, Teben'kov 2004). Outlined box shows the location of Figure 1b. BIS - Berzeliusegene Igneous Suite; BFZ - Billefjorden Fault Zone; BBFZ - Bockfjorden - Breibogen Fault Zone; ESZ - Eolusletta Shear Zone; RFZ - Raudfjorden Fault Zone; VKSZ - Vimsodden-Kosibapasset Shear Zone. (b) Geological map of central Oscar II Land (after Morris 1988; Dallmann 2015)

to ca. 410 Ma based on the unconformity between the Red Bay Group and the lower Andreé Land Group that has not been mapped in the field (Harland 1960; McCann 2000).

The boundary between SBP and the remaining provinces is unexposed (Gee, Teben'kov 2004). The SBP has a composite internal structure with multiple metamorphic and magmatic events unevenly overprinting basement blocks separated by Palaeozoic to Paleogene shear zones (e.g. Majka, Kośmińska 2017; Wala et al. 2021). In contrast to the other basement provinces of Svalbard as well as the North-East Greenland Caledonides, SBP is devoid of late Caledonian migmatization and post-orogenic felsic magmatism (Gee, Teben'kov 2004; Majka, Kośmińska 2017). Therefore, the inhomogeneity of the SBP led to several attempts to correlate its parts with the Pearya Terrane based on the Neoproterozoic metasedimentary successions and subduction-related Ordovician complexes (e.g. Gasser, Andresen 2013; Gee, Teben'kov 2004; Harland, Wright 1979; Ohta et al. 1989; Ohta 1994; Trettin 1987). Other authors emphasize the potential of the SBP being correlated with the Timanides due to the similarity of the Tonian-Cryogenian metasedimentary successions and late Cryogenian metamorphism (Majka et al. 2008, 2015; Mazur et al. 2009; Wala et al. 2021).

The SBP is characterized by two major Meso- to Neoproterozoic units. The first group is characterized by high-grade Cryogenian (ca. 640 Ma) and/or high-pressure Ordovician (ca. 480 Ma) metamorphism and consists of the Isbjørnhamna Group and Eimfjellet Groups (Majka et al. 2008), the Berzeliuseggene Unit (Majka et al. 2015) and the Vestgötabreen Complex (e.g. Hirajima et al. 1988; Barnes et al. 2020). The second group comprises most of the SBP, which was metamorphosed under greenschist facies conditions during the Ordovician-Silurian times (e.g. Manecki et al. 1998; Faehnrich et al. 2020). These two groups are separated from each other by either strike-slip faults (e.g. Majka et al. 2015; Mazur et al. 2009) or thrusts (e.g. Barnes et al. 2020). The timing of the strike-slip faults separating the remaining basement from the Eimfjellet Group and the Berzeliuseggene Unit has been dated to 424 ± 6 Ma and 410 ± 17 Ma, respectively (Faehnrich et al. 2020).

There are still two higher grade units in the SBP, namely the Kongsvegen Group and the Müllerneset Formation, that are poorly studied. The timing of metamorphism in these two units is still unknown, and their relationships with the remaining basement remain unclear due to the Paleogene-Neogene Eurekan overprint of older structures (e.g. Maher et al. 1997). According to the observed pattern in the southern part of SBP the age of prograde metamorphism in the Müllerneset Formation could be Torellian, but no geochronological evidence has been provided yet. This unit also has not been studied in the light of its relation to the concepts of Caledonian escape tectonics and the CATS, therefore it might provide new clues about the interaction of the two transcurrent fault systems.

2.1. Prins Karls Forland and Oscar II Land

The basement of Prins Karls Forland (PKF) is represented by the equivalent of the Sofiebogen Group (namely Ferrierpiggen, Geikie and Peachflya groups) overthrusting the Scotiafjellet and Grampianfjellet groups (Dallmann 2015; Kośmińska et al. 2020). The Grampianfjellet Group was thrusted during Eurekan Orogeny onto the amphibolite facies metasediments of the Pinkie unit (Kośmińska et al. 2020; Schneider et al. 2019). Strongly mylonitized Pinkie unit rocks were metamorphosed at ca. 370 - 355 Ma during Ellesmerian metamorphism (Kośmińska et al. 2020).

The oldest basement exposed in the eastern and northern parts of Oscar II Land (OIIL) consists of the Meso- to Neoproterozoic metasedimentary Kongsfjorden and St. Jonsfjorden groups (Harland, Wright 1979; Harland et al. 1993; Kanat, Morris 1988; Fig. 1b). These groups are composed of calcareous phyllites and marbles with overlying psammopelites intercalated by the Na-alkaline Trollheimen volcanics (Kanat, Morris 1988; Ohta 1985). The overlying Comfortlessbreen Group comprises Marinoan (Harland 1960; Harland 1997; Kanat, Morris 1988) or Gaskiers age tillite (Dallmann 2015) as well as calcareous schists and phyllites (Kanat, Morris 1988). The St. Johnsfjorden Group together with the Comfortlessbreen Group were metamorphosed under greenschist facies conditions during the Caledonian Orogeny (e.g. Ohta 1985). They are overthrust by the HP Vestgötabreen Complex and unconformably overlain the Ordovician to Silurian Bullbreen Group (Horsfield 1972; Kanat, Morris 1988; Labrousse et al. 2008; Ohta 1979; Ohta et al. 1983). The deposition of the Bullbreen Group occurred during the exhumation of the Vestgötabreen Complex based on the occurrence of HP clasts in Bullbreen conglomerate (Scrutton et al. 1976). The Bullbreen Group is bounded to the west by a zone of mixed lithologies called the 'chaotic zone' (Kanat, Morris 1988; Morris 1988). The 'chaotic zone' can be followed to the southeast and separates the Comfortlessbreen and St. Jonsfjorden groups from the Müllerneset Formation to the east (Gasser, Andresen 2013; Morris 1988).

Although separated by Forlandsundet, PKF and OIIL share a common deformation history. Previous workers recognized four stages of deformation (Manby 1986; Morris 1988; Piepjohn et al. 2000). Deformation phases D1 and D2 are characterized by nearly coaxial folds with fold axes trending NW-SE, and axial planes of F2 are steeper than axial planes of F1. On PKF, D1 is associated

with WSW thrusting refolded during D2 (Manby 1986). F1 and F2 show E vergences in OIIL, and their age was inferred to be pre-mid-Carboniferous (Morris 1988). D2 has affected the northward thrusted Vestgötabreen Complex and Bullbreen Group, which are characterized by different tectonometamorphic history prior to D2 (Labrousse et al. 2008; Michalski et al. 2014; Morris 1988). $^{40}Ar/^{39}Ar$ cooling age for Ordovician HP metamorphism yields ca. 476 - 461 Ma (Barnes et al. 2020; Dallmeyer 1989), whereas the juxtaposition of different HP units is interpreted as 454 ± 4 Ma (Barnes et al. 2020). Subsequent NNE-directed thrusting and folding at 430 Ma resulted in the formation of an E-W trending syncline (Barnes et al. 2020). The syncline was later overturned to ENE around Holmesletfjellet syncline of inferred late Silurian – Early Devonian (ca. 410 Ma) age and possibly coeval with D2 in the remaining basement (Labrousse et al. 2008; Michalski et al. 2014; Morris 1988). The local NNW-SSE trending dextral shearing and related thrusting recorded in the western Bullbreeen Group (Ratliff et al. 1988) can be attributed to the same event. Superimposed on the pre-mid-Carboniferous structures are D3 and D4, which are related to the development of the West Spitsbergen Fold and Thrust Belt (WSFTB) during the Eurekan deformation. D3 is characterized by the development of NE verging folds and thrusts in brittle to ductile regime, followed by NNW-SSE trending dextral strike-slip (e.g. Harland 1969; Hjelle et al. 1979; Maher et al. 1997; Piepjohn et al. 2016). D4 is represented by a system of brittle faults related to the Forlandsundet Graben formation along NNW-SSE bounding faults (e.g. Braathen et al. 1999; Piepjohn et al. 2016).

2.2. The Müllerneset Formation

In the western part of Oscar II Land, a thick metasedimentary succession of the Müllerneset Formation is exposed (Ague, Morris 1985; Dineley 1958; Harland, Wright 1979; Figs 1b; 2). It crops out on the Svartfjellstranda and the Svartfjella mountain range to the east, from St. Johnsfjorden to Eidembukta (Ague, Morris 1985, Figs 1b; 2). The northern part of the Müllerneset Formation is composed of phyllites, micaschists, garnet-micaschists and quartzites, with increasing quartzitic content to the west (Ague, Morris 1985). The southern part consists of more carbonaceous and chloritic lithologies, including calcareous phyllites, marbles, conglomerates and chlorite-garnet micaschists.

The Müllerneset Formation experienced a polymetamorphic history with multiple deformation episodes that were studied mostly in its northern part (Ague, Morris 1985). The main prograde metamorphic event M1 reaching the garnet zone of lower amphibolite facies is presumably of Caledonian age. Its peak metamorphic conditions were estimated to 6.6 kbar at ~535°C (Ague, Morris 1985). The highest grade lithology, garnet micaschists, occur locally in the easternmost and westernmost outcrops, while most of the Müllerneset Formation reached only the biotite zone of greenschist facies conditions. The contact between the garnet and biotite zone lithologies is gradational. Strong foliation S1 striking NW-SE with a steep to moderate SW dip and isoclinal folds with the NW-SE axes are related to the D1 event. The only observable map-scale F1 anticline was described in the western part of Svartfjellstranda (Ague, Morris 1985). Notably, there are also remnants of two earlier stages of mica growth predating S1 (Ague, Morris 1985). The geochronological data for the Müllerneset Formation are very limited. Single muscovite $^{40}Ar/^{39}Ar$ step heating age of 410 ± 2 Ma is interpreted as post peak metamorphic cooling (Dallmeyer 1989). The $^{40}Ar/^{39}Ar$ step heating also revealed an argon escape attributed to Eurekan deformation (Dallmeyer 1989).

The retrogressive metamorphic event M2 occurred synchronously with D2, and its effects are unevenly spread across the area (Ague, Morris 1985). Metamorphic conditions of M2 were lower than M1. Textures related to the fluid-aided retrogressive breakdown of garnet to chlorite and epidote are commonly observed. The D2 deformation is associated with crenulation and folds with angular geometries that are coaxial with the F1 fold axes (Ague, Morris 1985). The map-scale D2 anticline was inferred by Ague and Morris (1985) in the eastern part of Svartfjellstranda with the NW-SE trending axis and moderately to steeply dipping limbs. However, this structure is parallel to the main Svartfjella - Eidembukta - Daudsmannodden Lineament (SEDL) and may represent its western boundary fault as slivers of the Carboniferous crop out along the D2 anticline axis (Maher et al. 1997). D2 is therefore most likely associated with the Eurekan Orogeny prior to and during the displacement on SEDL dated at 67-49 Ma using K-Ar whole rock (Tessensohn et al. 2001).

3. Methods

3.1. Mineral chemistry and element maps

Wavelength dispersive spectroscopy (WDS) analysis of mineral chemical composition was performed using a JEOL JXA-8230 Superprobe electron probe microanalyzer at Critical Elements Laboratory of Faculty of Geology, Geophysics and Environmental Protection, AGH - University of Science and Technology in Kraków, Poland. The operating conditions were as follows: 15 kV accelerating voltage, 20 nA beam current, counting times 20 s on peaks and 10 s on background positions. The beam

diameter was 1 µm for garnet and ilmenite analyses and 5 µm for the remaining minerals. The following standards were used for calibration of all detected silicates: orthoclase (Si Kα, K Kα), TiO_2 (Ti Kα), metallic Cr (Cr Kα), Al_2O_3 (Al Kα), fayalite (Fe Kα), rhodonite (Mn Kα), forsterite (Mg Kα), wollastonite (Ca Kα), albite (Na Kα). For allanite-(Ce) and bastnäsite-(Ce) following standards were used for calibration with adjusted counting times on peaks: 20s for albite (Si Kα, Na Kα, Al Kα), diopside (Mg Kα, Ca Kα), $CePO_4$ (P Kα, Ce Lα), hematite (Fe Kα), Cr_2O_3(Cr Kα), rhodonite (Mn Kα), rutile (Ti Kα), celestine (Sr Lα), ThO_2 (Th Mα), UO_2 (U Mβ), $LaPO_4$ (La Lα), $NdPO_4$ (Nd Lα), $SmPO_4$ (Sm Lα), krokoite (Pb Mβ), $AlAsO_4$ (As Lα); 30 s for $PrPO_4$ (Pr Lβ); 40 s for anhidrite (S Kα), YPO_4, (Y Lα), metallic Sc (Kα), metallic vanadium (V Kα), $GdPO_4$ (Gd Lβ), $TbPO_4$ (Tb Lα), $DyPO_4$ (Dy Lα), $HoPO_4$ (Ho Lβ), $ErPO_4$ (Er Lα), $TmPO_4$ (Tm Lα), $LuPO_4$ (Lu Lα); 60 s for $EuPO_4$ (Eu Lα). The PAP corrections were applied for the matrix effects. The mineral abbreviations are according to Whitney and Evans (2010) but WM - white mica.

X-ray compositional maps of garnet were obtained using the same instrument. The measurement conditions were: 15 kV accelerating voltage, 100 nA beam current, step size 1.5 µm and dwell time of 100 ms. Chemical maps of Mg Kα, Ca Kα, Ti Kα, and Mn Lα were collected. The element ratios were determined from the cation distribution scans using XMapTools 2.4.3 (Lanari et al. 2014; 2019). Cut-off limits were selected to correspond with the spread of the values.

3.2. Th-U-total Pb monazite dating

Chemical dating of monazite was performed using a CAMECA SX-100 electron probe microanalyzer at the

Table 1. Representative chemical analysis of garnet and biotite. Structural formulae recalculated on the basis of 12 and 11 oxygens, respectively.

Mineral	Grt	Grt	Grt	Grt	Bt-I	Bt-I	Bt-II	Bt-II	Bt-II
Analysis	Grt4	Grt7	Grt5	Grt9	bt4	bt8	bt9	bt11	bt12
Position	core	core	rim	rim	matrix	matrix	matrix	matrix	shadow
SiO_2	37.71	36.92	36.76	36.91	34.68	34.28	34.40	35.09	33.67
TiO_2	0.10	0.09	0.12	0.04	1.85	1.81	1.75	1.77	1.18
Al_2O_3	20.87	20.85	20.73	21.00	18.68	18.67	18.49	18.62	19.26
Cr_2O_3	0.02	0.01	0.01	0.00	0.01	0.03	0.04	0.02	0.00
FeO	29.94	36.13	27.51	35.96	22.52	23.20	22.87	22.88	22.97
MnO	4.75	0.52	7.31	0.41	0.01	0.10	0.04	0.02	0.07
MgO	0.74	1.30	0.64	1.46	7.30	6.85	7.24	6.93	6.98
CaO	6.31	4.26	6.01	4.10	0.00	0.01	0.01	0.01	0.00
Na_2O	0.00	0.04	0.02	0.01	0.20	0.05	0.13	0.12	0.13
K_2O	0.00	0.02	0.00	0.00	8.87	8.98	8.83	9.09	8.91
Total	100.42	100.12	99.10	99.90	94.11	93.98	93.80	94.53	93.19
Si	3.037	2.988	3.003	2.991	2.710	2.697	2.704	2.734	2.671
Ti	0.006	0.006	0.007	0.002	0.109	0.107	0.104	0.103	0.071
Al	1.982	1.990	1.997	2.007	1.721	1.732	1.714	1.710	1.801
Cr	0.001	0.001	0.000	0.000	0.001	0.002	0.002	0.001	0.000
Fe^{2+}	2.017	2.446	1.880	2.437	1.472	1.526	1.503	1.491	1.524
Mn	0.324	0.036	0.506	0.028	0.001	0.006	0.002	0.001	0.005
Mg	0.088	0.157	0.078	0.176	0.851	0.803	0.849	0.805	0.825
Ca	0.544	0.369	0.526	0.356	0.000	0.001	0.001	0.001	0.000
Na	0.000	0.006	0.002	0.002	0.031	0.007	0.020	0.018	0.020
K	0.000	0.002	0.000	0.000	0.884	0.901	0.886	0.903	0.902
total	7.977	8.010	7.990	8.002	7.778	7.783	7.787	7.768	7.819
Ox base	12	12	12	12	11	11	11	11	11
X_{Alm}	0.68	0.81	0.63	0.81					
X_{Sps}	0.11	0.01	0.17	0.01					
X_{Prp}	0.03	0.05	0.03	0.06					
X_{Grs}	0.18	0.12	0.18	0.12					
X_{Fe}	0.96	0.94	0.96	0.93	0.63	0.66	0.64	0.65	0.65
Al^{VI}					0.43	0.43	0.42	0.44	0.47

Table 2. Representative chemical analysis of muscovite, plagioclase, ilmenite and chlorite. Structural formulae recalculated on the basis of 11, 8, 3 and 14 oxygens, respectively.

Mineral	Ms-I	Ms-II	Ms-II	Msl/II	Pl	Pl	Ilm	Ilm	Ilm	Ilm	Chl
Analysis	wm2	wm1	wm3	wm4	Ab1	Ab2	ilm9	ilm10	ilm12	ilm14	chl4
Position	matrix	matrix	matrix	shadow	core	rim	matrix	in Grt	in Grt	matrix	shadow
SiO_2	46.86	46.09	46.02	46.37	67.64	65.55	0.01	0.02	0.01	0.04	23.71
TiO_2	0.32	0.24	0.27	0.26	0.01	0.00	53.07	53.72	52.75	52.57	0.16
Al_2O_3	32.38	34.64	35.01	33.78	19.71	21.16	0.01	0.00	0.07	0.07	21.50
Cr_2O_3	0.04	0.03	0.00	0.01	0.00	0.00	0.00	0.00	0.00	0.00	0.04
FeO	2.08	1.65	1.75	1.95	0.29	0.24	44.91	45.10	45.47	44.61	31.67
MnO	0.02	0.00	0.02	0.00	0.03	0.00	1.68	1.50	2.37	0.84	0.12
MgO	1.35	0.77	0.75	1.07	0.00	0.00	0.00	0.00	0.00	0.00	9.84
CaO	0.00	0.00	0.03	0.01	0.09	1.63	0.14	0.01	0.13	0.00	0.02
Na_2O	0.66	0.90	0.90	0.84	11.77	10.71	0.00	0.00	0.00	0.04	0.03
K_2O	9.90	9.78	9.60	9.72	0.06	0.08	0.00	0.10	0.01	0.13	0.00
Total	93.61	94.09	94.33	94.02	99.60	99.40	99.82	100.44	100.80	98.32	87.09
Si	3.177	3.101	3.087	3.127	2.964	2.89	0.000	0.001	0.000	0.001	2.613
Ti	0.016	0.012	0.014	0.013	0.000	0.000	1.010	1.016	0.993	1.015	0.013
Al	2.588	2.748	2.769	2.686	1.018	1.101	0.000	0.000	0.002	0.002	2.794
Cr	0.002	0.002	0.000	0.001	0.000	0.000	0.000	0.000	0.000	0.000	0.003
Fe^{2+}	0.118	0.093	0.098	0.110	0.010	0.009	0.950	0.948	0.951	0.958	2.919
Mn	0.001	0.000	0.001	0.000	0.000	0.000	0.036	0.032	0.050	0.018	0.012
Mg	0.137	0.077	0.075	0.107	0.000	0.000	0.000	0.000	0.000	0.000	1.617
Ca	0.000	0.000	0.002	0.001	0.004	0.077	0.004	0.000	0.004	0.000	0.003
Na	0.087	0.117	0.117	0.109	1.000	0.916	0.000	0.000	0.000	0.002	0.007
K	0.857	0.840	0.821	0.836	0.003	0.005	0.000	0.003	0.000	0.004	0.000
Total	6.983	6.990	6.983	6.990	4.999	5.001	2.000	2.000	2.000	2.000	9.979
Ox base	11	11	11	11	8	8	3	3	3	3	14
X_{Ab}					0.993	0.918					
X_{Mn}							0.03	0.03	0.05	0.01	

State Geological Institute of Dionỳz Štúr in Bratislava, Slovakia. Counting times were increased from the ones used for chemical composition analysis to 80 s for U and 300 s for Pb to meet the laboratory requirements for trace element analysis. The beam current was adjusted to 180 nA and spots were measured with a 3 μm beam diameter. The detection limits were 225 ppm for Th, 205 ppm for U and 95 ppm for Pb. The following standards were used for calibration: barite (S Kα) apatite (P Kα), GaAs (As Lα), ThO_2 (Th Mα), UO_2 (U Mβ), Al_2O_3 (Al Kα), YPO_4, (Y Lα), $LaPO_4$ (La Lα), $CePO_4$ (Ce Lα), $PrPO_4$ (Pr Lβ), $NdPO_4$ (Nd Lβ), $SmPO_4$ (Sm Lβ), $EuPO_4$ (Eu Lβ), $GdPO_4$ (Gd Lα), $TbPO_4$ (Tb Lα), $DyPO_4$ (Dy Lβ), $HoPO_4$ (Ho Lβ), $ErPO_4$ (Er Lβ), $TmPO_4$ (Tm Lα), $YbPO_4$ (Yb Lα), $LuPO_4$ (Lu Lβ), $SrTiO_3$ (Sr Lα), fayalite (Fe Kα), wollastonite (Ca Kα, Si Kα), and $PbCO_3$ (Pb Mα). Empirically determined correction factors were applied to the following line overlaps: Th→U, Dy→Eu, Gd→Ho, La→Gd, Ce→Gd, Eu→Er, Gd→Er, Sm→Tm, Dy→Lu, Ho→Lu, Yb→Lu, and Dy→As (Konečný et al. 2004). Spot analyses of monazite were corrected for mutual interferences (see Konečný et al. 2004; 2018; Petrík, Konečný 2009), and then the weighted average of apparent ages was calculated following the statistical method of Montel et al. (1996). The matrix effects were corrected using the Pouchou and Pichoir (1991) procedure. Representative chemical analyses of all minerals from sample PSD03 are presented in Tables 1 and 2.

4. Results

4.1. Field observations

Structural and petrological observations are in part consistent with those made by Ague and Morris (1985). Mapping of the area showed that in the core of the F2 anticline slivers of unmetamorphosed rocks resembling the Carboniferous Gipsdalen Group can be found (Fig. 2). These slivers are present on the map of Maher et al. (1997), while Krasil'ščikov et al. (1995) interpret the anticline core as inferred fault parallel to the SEDL (Maher et al. 1997). Inferred fault divides the rocks of the Müllerneset For-

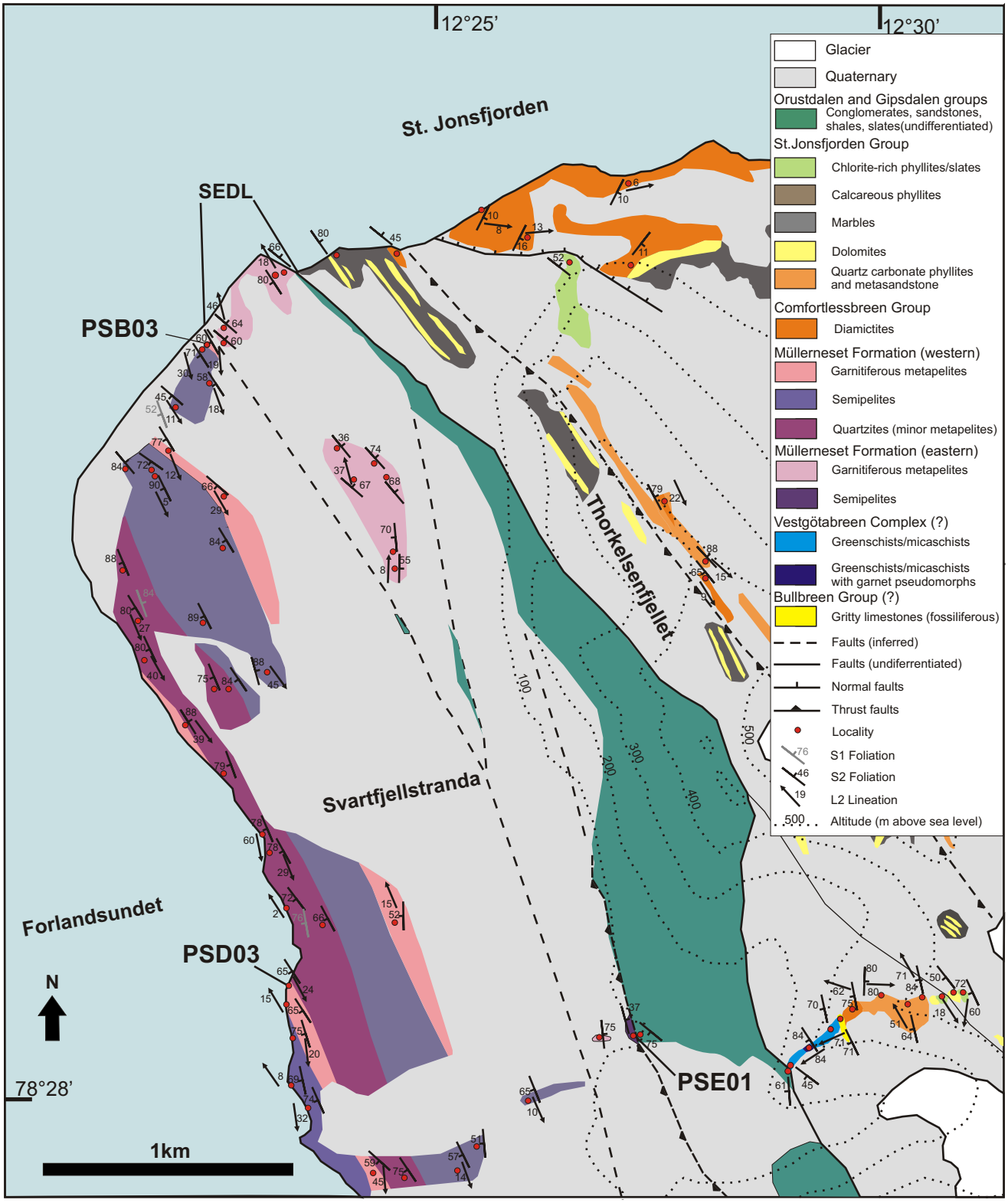

Figure 2. Schematic geological map of Svartfjellstranda area (Ague, Morris 1988; Maher et al. 1997; Dallmann 2015, modified).

mation into two tectonic blocks – western and eastern. The examined rocks of the Müllerneset Formation show evidence of two metamorphic events with accompanying distinctive foliations (Figs 3; 4a, b). The first event is associated with the development of a lower amphibolite facies paragenesis of garnet + biotite + quartz + muscovite + plagioclase ± carbonates ± graphite. The second event is lower grade and defined by paragenesis of biotite + chlorite + quartz + muscovite + plagioclase ± carbonates. Early foliation (S1) related to the first event (M1) is observed as segregation into metapelitic, quartzofeldspathic and quartzitic domains and within them, defined by biotite and graphite that may represent original sedimentary bedding (Fig. 4a). The foliation can be observed mainly as centimetre to metre-scale microlithons. A secondary foliation (S2) is defined by a newly formed penetrative mylonitic foliation, a transposed S1 foliation, or as axial planes of folds affecting S1 (Fig. 4a-d). S2 is defined by biotite, muscovite and chlorite in both metapelitic and quartzofeldspathic domains. The strong fabric

Table 3. Representative chemical analysis of apatite, allanite-(Ce) and bastnäsite. Structural formulae recalculated on the basis of 3, 12 and 21 oxygens, respectively.

Mineral	Ap	Aln	Aln	Bst	Bst		Ap	Aln	Aln	Bst	Bst
Analysis	Ap1	aln1	aln2	bst1	bst2		Ap1	aln1	aln2	bst1	bst2
Position	matrix	matrix	matrix	matrix	matrix		matrix	matrix	matrix	matrix	matrix
SO_3	0.00	0.01	0.00	0.00	0.19	S	0.000	0.001	0.000	0.001	0.042
P_2O_5	42.88	0.01	0.06	0.03	0.09	P	3.019	0.000	0.005	0.008	0.021
As_2O_5	n.a.	0.03	0.01	0.00	0.00	As		0.002	0.001	0.000	0.000
SiO_2	0.08	31.54	30.64	0.30	1.00	Si	0.007	2.936	2.889	0.091	0.297
TiO_2	n.a.	0.25	0.35	0.07	0.02	Ti		0.017	0.025	0.016	0.004
ThO_2	n.a.	0.03	0.23	0.88	1.25	Th		0.001	0.005	0.061	0.085
UO_2	n.a.	0.13	0.12	0.15	0.00	U		0.003	0.002	0.011	0.000
Al_2O_3	0.04	16.90	16.49	0.03	0.04	Al	0.004	1.854	1.832	0.009	0.015
Sc_2O_3	n.a.	0.00	0.00	0.02	0.04	Sc		0.000	0.000	0.005	0.011
V_2O_3	n.a.	0.18	0.08	0.00	0.00	V		0.013	0.006	0.000	0.000
Cr_2O_3	n.a.	0.06	0.15	0.04	0.03	Cr		0.005	0.011	0.010	0.007
Fe_2O_3	-	15.11	14.76	0.53	0.52	Fe^{3+}		1.058	1.047	0.121	0.117
FeO	0.22	-	-	-	-	Fe^{2+}	0.015				
Y_2O_3	0.05	0.19	0.12	0.68	0.51	Y	0.002	0.009	0.006	0.111	0.081
La_2O_3	0.21	5.99	5.71	15.89	15.98	La	0.006	0.206	0.198	1.793	1.758
Ce_2O_3	0.03	12.65	12.41	30.96	28.94	Ce	0.001	0.431	0.428	3.468	3.159
Pr_2O_3	0.03	1.37	1.37	3.58	3.38	Pr	0.001	0.047	0.047	0.399	0.367
Nd_2O_3	0.03	4.10	4.70	14.15	12.68	Nd	0.001	0.136	0.158	1.546	1.350
Sm_2O_3	0.00	0.46	0.76	2.03	1.98	Sm	0.000	0.015	0.025	0.214	0.204
Eu_2O_3	n.a.	0.08	0.09	0.35	0.38	Eu		0.002	0.003	0.036	0.039
Gd_2O_3	0.16	0.12	0.40	1.28	1.29	Gd	0.005	0.004	0.013	0.130	0.127
Tb_2O_3	n.a.	0.12	0.10	0.17	0.14	Tb		0.004	0.003	0.017	0.014
Dy_2O_3	n.a.	0.04	0.07	0.20	0.21	Dy		0.001	0.002	0.020	0.020
Ho_2O_3	n.a.	0.00	0.00	0.07	0.00	Ho		0.000	0.000	0.007	0.000
Er_2O_3	n.a.	0.11	0.07	0.03	0.11	Er		0.003	0.002	0.003	0.011
Tm_2O_3	n.a.	0.00	0.11	0.26	0.21	Tm		0.000	0.003	0.025	0.020
Yb_2O_3	n.a.	0.02	0.07	0.05	0.00	Yb		0.001	0.002	0.004	0.000
Lu_2O_3	n.a.	0.07	0.02	0.00	0.00	Lu		0.002	0.001	0.000	0.000
MgO	0.00	0.20	0.13	0.00	0.00	Mg	0.000	0.028	0.018	0.000	0.000
CaO	54.88	8.43	9.03	0.58	1.63	Ca	4.891	0.841	0.912	0.189	0.522
MnO	0.00	0.21	0.32	0.00	0.07	Mn	0.000	0.017	0.026	0.000	0.017
SrO	0.06	0.04	0.02	0.31	0.31	Sr	0.003	0.002	0.001	0.055	0.054
PbO	0.00	0.02	0.00	0.04	0.01	Pb	0.000	0.001	0.000	0.003	0.001
Na_2O	0.00	0.07	0.07	0.00	0.03	Na	0.001	0.013	0.012	0.000	0.019
F	1.26	0.00	0.00	4.22	2.86	F	0.322	0.000	0.000	3.078	2.215
Cl	0.00	n.a.	n.a.	n.a.	n.a.	Cl	0.000				
Total	99.93	98.53	98.46	75.10	72.69	Total	8.277	7.651	7.684	11.428	10.574
						Ox base	12	12	12	21	21

of the S2 with decreased grain size is developed mainly in the metapelitic domains, while quartzofeldspathic ones remain rigid forming recrystallizing microlithons or rootless folds (Fig. 4a). In the majority of outcrops S1 is transposed into S2, and the angle between them if existent, is usually very low, making them difficult to distinguish (Fig. 4a, b). Locally ductile S-C and S-C-C' structures can be observed, where S2 foliation corresponds to C2 planes and is often affected by sinistral C2' shear bands (Fig. 4b). The C2' are locally reactivated under brittle conditions. Rarely S1 intersection lineation with S2 is observed in quartzofeldspathic domains and usually steeply plunging or reoriented towards the direction of L2 lineation. S2 is associated with stretching lineation

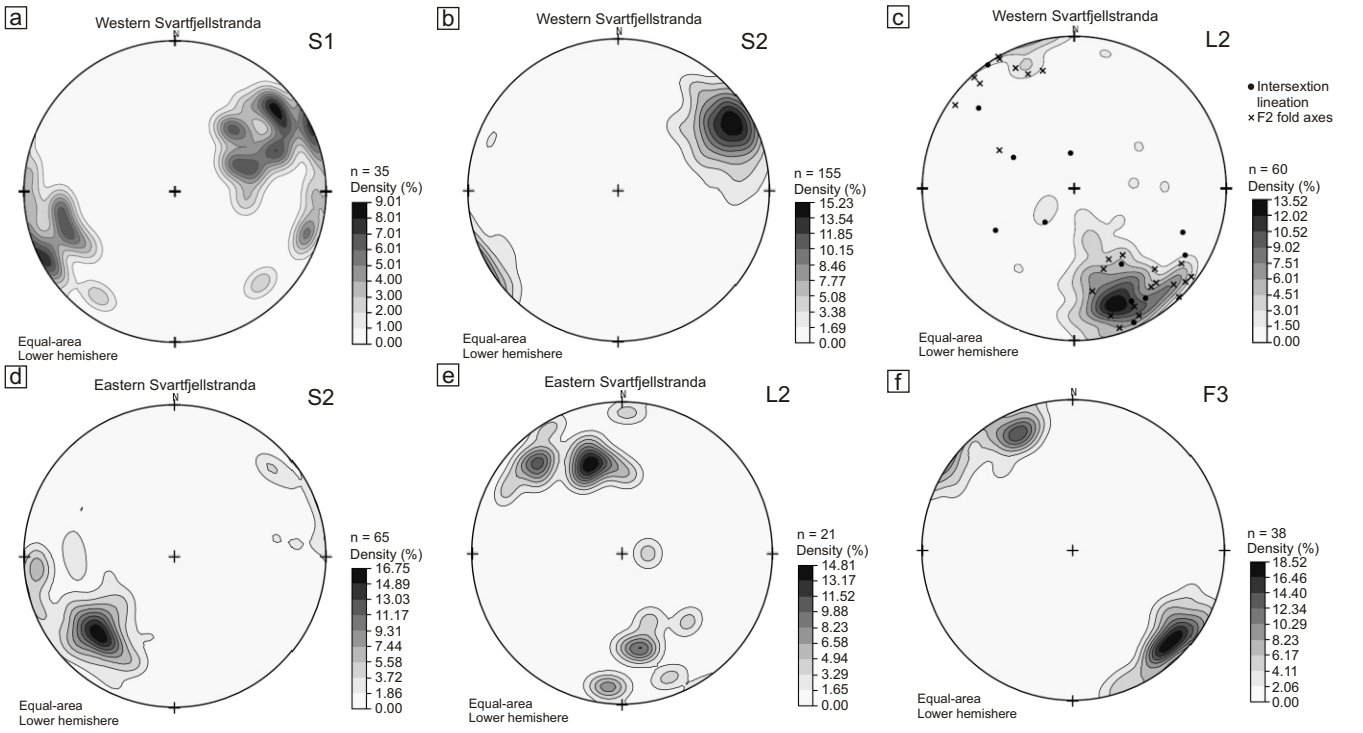

Figure 3. Structural features of studied areas presented on stereonets - equal area, lower hemisphere. Western Svartfjellstranda (a) poles S1, (b) poles to mylonitic S2, S1/S2 intersection lineation and F2 fold axes, (c) attitudes of L2; Eastern Svartfjellstranda (d) poles to mylonitic S2, (e) attitudes of L2; Svartfjellstranda (f) attitudes of F3 axes.

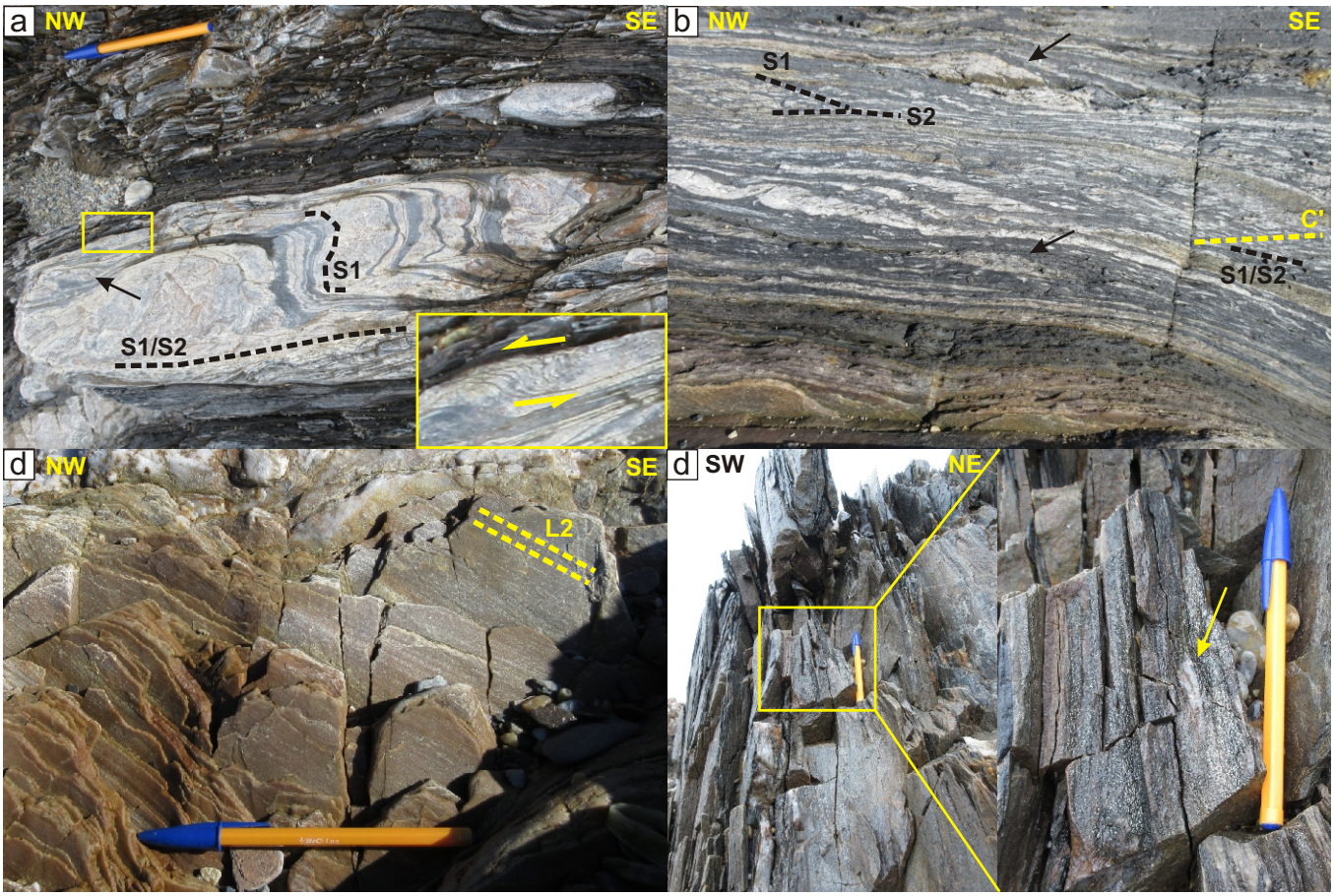

Figure 4. Structures of Western Svartfjellstranda (a) S1 preserved in a microlithon and progressively sheared into parallelism with S2 along boundaries of the quartzofeldspathic domain. Drag folds consistent with the sense of shear marked by an arrow. The rectangle marks a close-up of a microduplex. (b) Relationships of S1 and S2 foliations in the local shear zone with apparent S-C-C' structures and increasing shear gradient towards SW. Black arrows mark asymmetric and recrystallized quartzofeldspathic microlithons. (c) L2 muscovite bearing stretching lineation. (d) F2 fold with associated biotite lineation. Note rootless infolded quartz vein marked by an arrow.

defined by the orientation of quartzofeldspathic aggregates with mineral lineation (L2) defined by biotite and muscovite (Fig. 4c, d). L2 lineations are colinear with tight to isoclinal folds (F2) defined by folded boundaries between quartzofeldspathic and metapelitic domains – S1 foliation (Fig. 4d).

The structures related to the semi-brittle deformation event are unevenly distributed across the area. Open angular folds (F3) refolding F2 folds are associated with spaced crenulation cleavage. The F3 axes and associated crenulation lineation are predominantly plunging shallowly toward the SW-NE direction (average 140/8; Figs 3f; 5d). The youngest brittle deformation is associated with brittle normal faults striking toward the ENE-WSW direction.

Variation of the observed S2 and L2 attitudes led to a division of the field area into western and eastern domains (Figs 2; 3). The boundary between the domains follows the SEDL parallel fault inferred by Krasil'ščikov et al. 1995. A short summary of the observed structures and parageneses is presented in Table 4.

4.1.1. Western Svartfjellstranda

The western part of the Müllerneset Formation is dominated by interlayered micaschists, garnet micaschists and quartzites. Discontinuous layers of the garnetiferous lithologies are present in the westernmost and easternmost outcrops and are separated by micaschists and quartzites. The quartzite-dominated lithologies mainly crop out in the western part along the coast.

S1 is preserved only in microlithons (Fig. 3a). The steep retrograde S2 is dipping toward the WSW-SW with an average orientation of 242/73 (Figs 2; 3b). The S2 is accompanied by L2 lineation plunging moderately to shallowly toward the SE-SSE with an average orientation of 160/21 (Figs 3c; 4c, d). Inferring map-scale structures is impossible due to the lack of proper correlative marker horizons. The general trend of lithological boundaries at the map scale follows the trend of S2 (Fig. 2).

The isoclinal F2 folds have a direction consistent with the stretching lineation. However, in the westernmost outcrops the folds are frequently rootless and show variable plunge values (Fig. 4b, d). Macroscopic kinematic indicators including sheared microlithons and post-D1 quartz veins, boudinage, flanking and thickening structures are consistent with left-lateral shearing (Figs 4a, b; 5a, b). Toward the east shear gradient decreases gradually with a distinguishable S1 foliation being folded by isoclinal and tight F2 folds within the metapelitic domains (Fig. 5c). The structures related to the D3 brittle to ductile deformation event are more common near the boundary with the eastern part of the area.

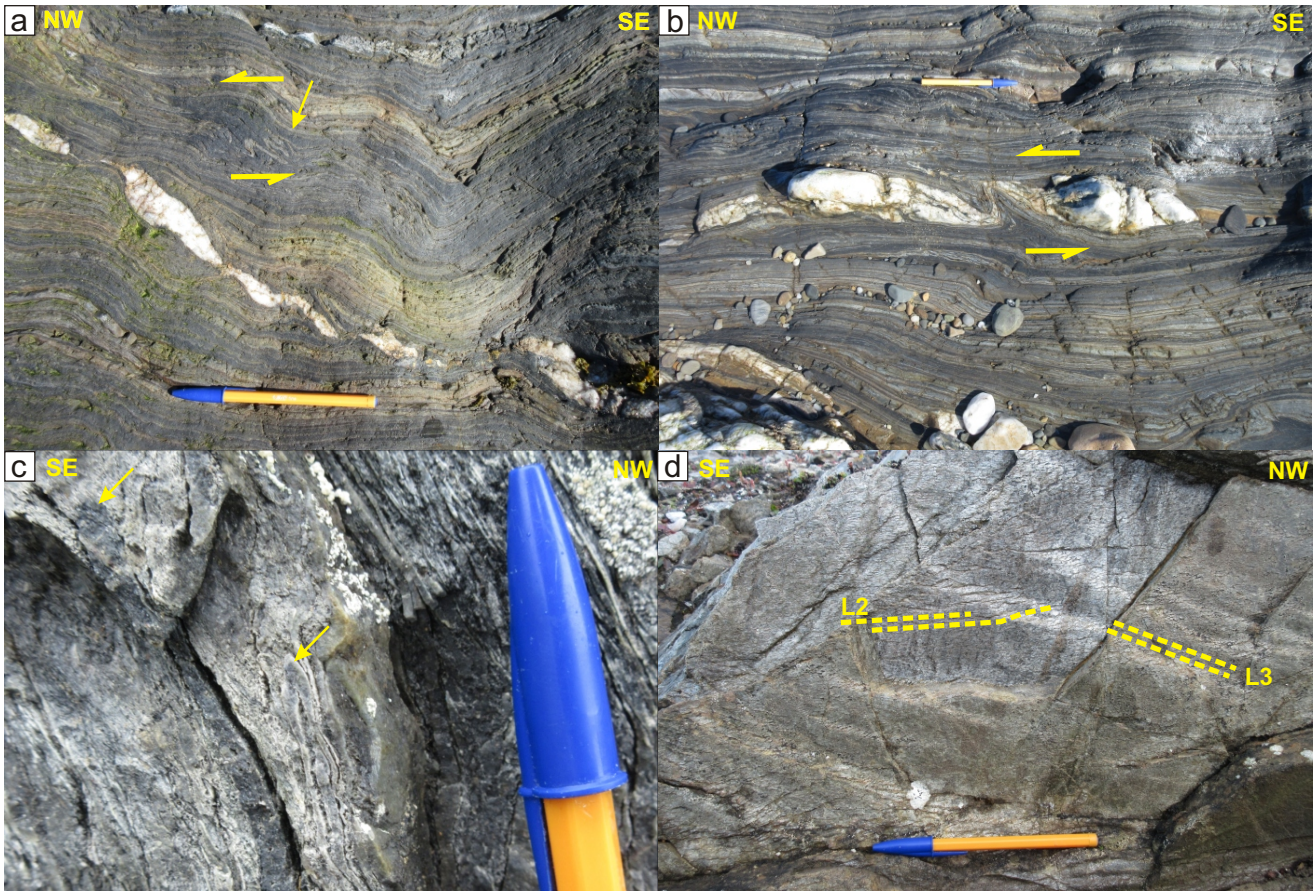

Figure 5. Structures of Western Svartfjellstranda cont. (a-b) left-lateral sense of shear kinematic indicators: (a) Boudinaged post D1 quartz vein giving rise to a flanking structure. Above contractional shear transfer structure marked by an arrow. (b) Boudinaged post D1 quartz vein. (c) F2 isoclinal folds with axial S2 foliation. (d) L2 stretching lineation folded around L3 crenulation associated with open F3 folds.

4.1.2. Eastern Svartfjellstranda

The boundary between the western and eastern parts of the Müllerneset Formation is unexposed. However, several blocks of Carboniferous sandstones on the strandflat (Fig. 2) suggest that it may represent a western boundary fault that belongs to the SEDL (Maher et al. 1997) similarly to the localities farther to the south in OIIL. To the east Müllerneset Formation is bounded by various lithologies that belong to the Carboniferous Orustdalen and Gipsdalen groups. The boundary is tectonized, although karstified micaschists with magnetite and hematite are observed on the boundary between the Müllerneset Formation and the Carboniferous, suggesting an unconformable contact (Fig. 6a, b) as it is observed further South (Maher et al. 1997).

The eastern part of the Müllerneset Formation is composed of micaschists with garnet commonly replaced by chlorite. S1 is observed mainly in centimetre-scale microlithons as quartzofeldspathic domains that are much thinner (Fig. 6c, d). In contrast to the western Svartfjellstranda, S2 displays a moderate to steep dipping towards the NE (Figs 3c; 6c-d), and the L2 stretching and mineral lineation are plunging shallowly to moderately towards the NNW-SSE or NW-SE, showing more variable spread than in western Svartfjellstranda (Figs 3d; 6d). The eastern part of the Müllerneset Formation lacks large-scale quartzite lenses and quartz veins, therefore no large-scale kinematic indicators have been observed, but sheared microlithons and dynamically (re)crystallized mica and chlorite around garnet as well as garnet pressure shadows show top to SE (Fig. 6c) or right lateral sense of shear (Fig. 6d). S2 is locally folded by open to tight F3 folds with axes plunging mainly towards the SE and axial planes dipping variably toward the NE. Lack of marker horizons and poor exposure of the Müllerneset Formation do not allow for the tracing of continuous large-scale structures, but variations in the dip of S2 along NW-SE transects suggest that there is some local rotation around F3 (Figs 2; 3e).

4.2. Petrography and mineral chemistry

The samples containing monazite larger than 3 µm were selected for further petrological analysis because such grains can be dated using the Th-U-total Pb method.

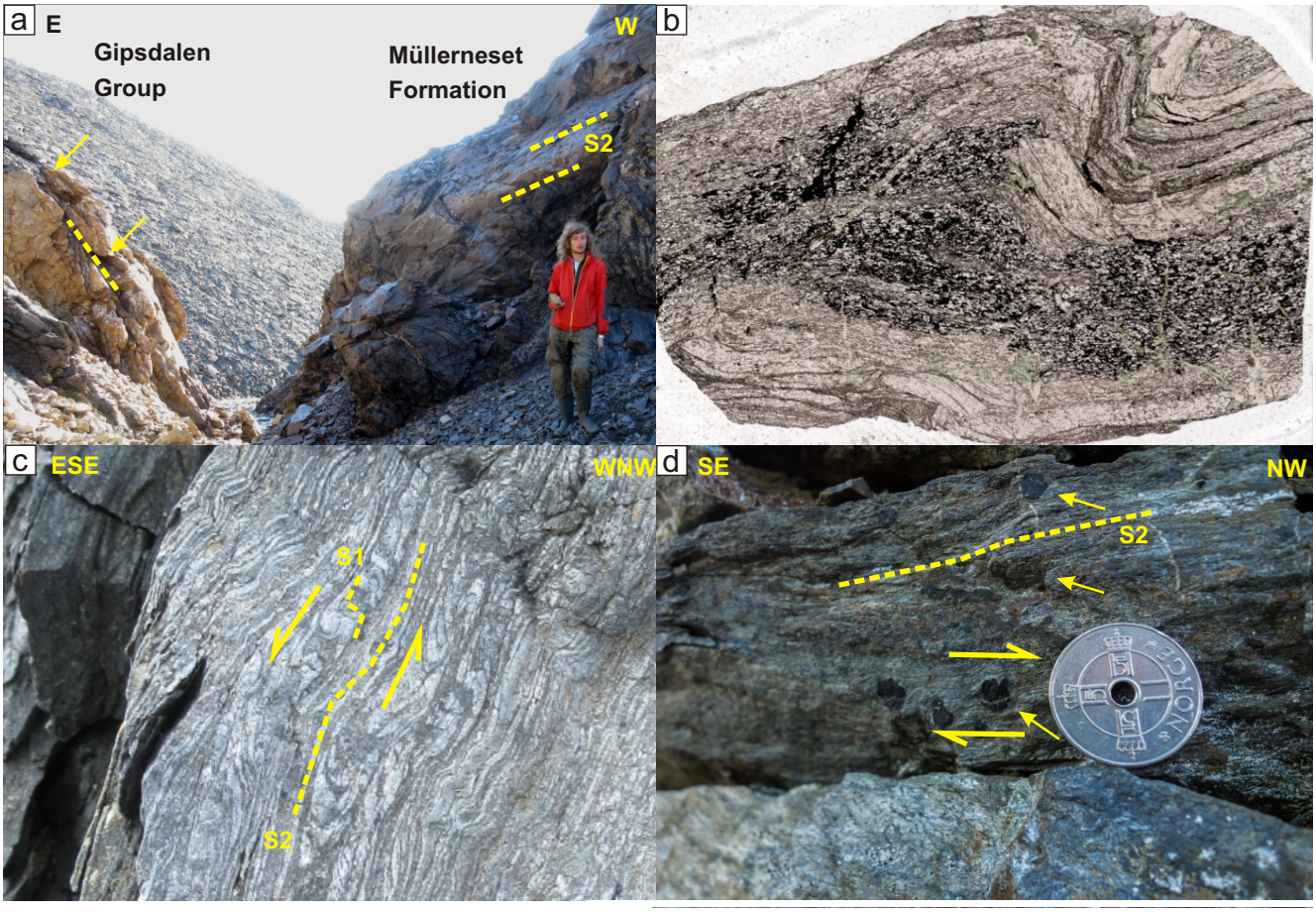

Figure 6. Structures of Eastern Svartfjellstranda. (a) Contact of Müllerneset Formation and the Gipsdalen Group. Note the angle between S2 foliation dipping moderately to NE in the Müllerneset Formation and S0/S1 dipping steeply to SW in the Gipsdalen Group. Arrows mark brittle F3 tight fold hinges in the Carboniferous. (b) Scanned thin section of the Müllerneset Formation in contact with the Gipsdalen Group in the PSE01 locality (Fig. 2). Evidence of karstification with the formation of magnetite and hematite marks a boundary between ductile D2 in Müllerneset and brittle D3 in the Carboniferous. (c) S1 microlithons sheared into parallelism with S2 foliation. Sense of shear is right-lateral/top-to-W; the height of the photo is approximately 5 cm. (d) Garnet with accompanying asymmetric muscovite and chlorite dynamic recrystallization indicating the dextral sense of shear (yellow arrows).

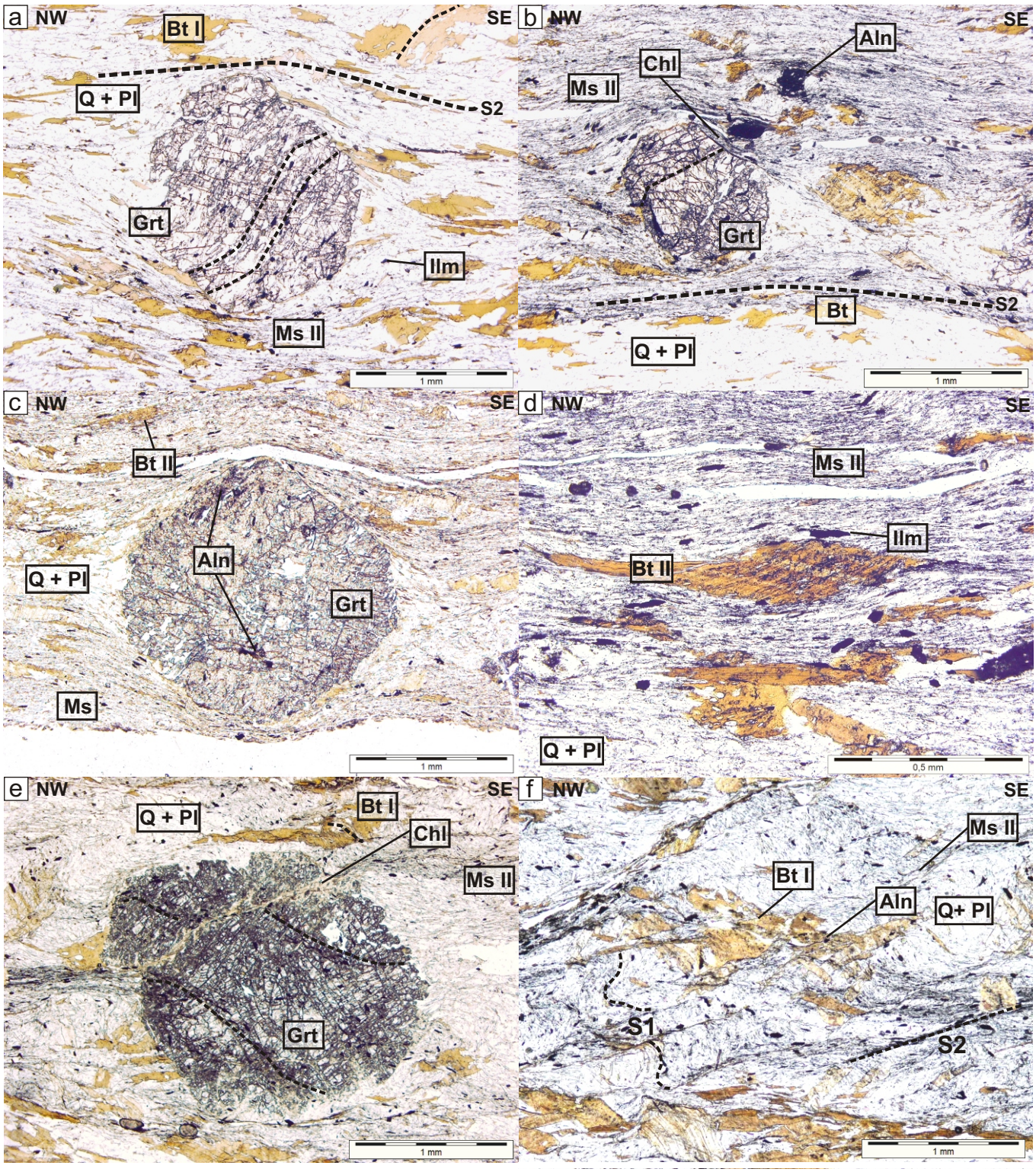

Figure 7. Photomicrographs of samples PSD03 and PSB03 in plane-polarized light presenting relationships between M1 and M2 parageneses in samples PSD03 (a-d) and PSD03 (e-f). The view is in plane ~240/25/SE. Kinematic indicators for D2 associated with M2 are consistently left-lateral in all photomicrographs. (a) M1 assemblage, inclusion trails in garnet, and biotite porphyroclasts rotated in the rim with a left-lateral sense of shear. (b) Pressure shadows developed around M1 porphyroclasts of garnet, biotite and allanite-(Ce) porphyroclasts. The garnet porphyroclast is broken and translated along the dashed line. (c) Allanite-(Ce) included in garnet porphyroclast. (d) Biotite-II porphyroclasts with left laterally rotated inclusion trails. (e) Garnet with inclusion trails in the rim rotated with the right-lateral sense of shear. The left-lateral displacement of the garnet along S2 highlighted by chlorite. (f) interaction between S1 foliation and S2 foliation (shear bands).

Only two samples, PSDO3A and PSBO3A, out of 24 total samples collected met this criterion and were studied in detail – both of them were collected from the western part of Svartfellstranda (Fig. 2). Representative chemical analyses of all minerals were conducted only for sample PSD03A as both garnet and biotite from PSB03A experienced heavy retrogression and the peak P-T minerals are not present. These representative chemical analyses are presented in Tables 1-3.

The samples consist of micaceous and quartzofeldspathic domains alternating in order of hundreds of micrometres to several millimetres. The M1 assemblage

Table 4. Summary of the metamorphic and deformational events observed in the Müllerneset Formation.

	D1/M1		D2/M2		D3 and later
	Early	Peak	Western Svartfjella	Eastern Svartfjella	
Type of deformation	ductile-greenschist facies	ductile-amphibolite facies	Ductile-greenschist facies	ductile greenschist facies	ductile to brittle
Metamorphic Assemblage	Bt+Ms+ Pl+Q	Grt+Bt-I+Ms-I+Pl+Q	Bt-II+Ms-II+Chl+Pl+Q	Bt-II+Ms-II+Chl+Pl+Q	-
Foliation	-	metamorphic segregation steep NE-SW dipping	defined by phyllosilicates mylonitic steep SW dipping	defined by phyllosilicates mylonitic steep to moderate NE dipping	defined by fold axial planes steep NE dipping
Structures	-	remained only in micro-lithons	tight to isoclinal folds S-C-C' structures	tight to isoclinal folds S-C-C' structures	open folds angular folds
Kinematic indicators	-	inclusion trails in Grt minor pressure shadows *sinistral/dextral*	multiple *dominant sinistral*	multiple *dominant dextral*	on SEDL - *dominant dextral*
REE minerals	monazite	allanite	monazite bastnäsite?	monazite bastnäsite?	bastnäsite?
Age	ca. 450 Ma ?	-	410 ± 8 Ma	as in western	Pg-Ng

in both samples comprises muscovite + quartz + biotite + plagioclase + garnet + ilmenite + allanite with accessory epidote, zircon, tourmaline and apatite (Fig. 7a-f). Allanite is preserved as inclusions both in garnet and biotite, as well as up to 0.4 mm aggregates in the matrix (Fig. 7b, c). S1 is preserved as quartz and ilmenite inclusion trails in pre-to synkinematic porphyroblasts, biotite alignments in the quartzofeldspathic domains and in the domains between younger shear bands (sample PSB03A, Fig. 7e, f). The inclusion trails in garnet often do not continue into the matrix and show the opposite sense of S1 displacement between the samples PSD03A and PSB03A, with the former displaying sinistral apparent (Fig. 7a-c) and the latter displaying apparent dextral rotation (Fig. 7e; Table 4).

The M2 assemblage consists of muscovite + quartz + chlorite + biotite + plagioclase + ilmenite + monazite (Fig. 7d). In both samples S2 has a strike of 330-335°, dipping 65-60° to SW and is highlighted by muscovite, biotite and ilmenite blasts wrapping around garnet, biotite and allanite porphyroclasts as well as forming pressure shadows around them (Fig. 6a-f). In sections perpendicular to S2 and parallel to L2 (i.e. 240/25/SE) in both samples the kinematic indicators were developed under a left-lateral regime. That includes the orientation of pressure shadows (Fig. 7a, b, f), shear zones developed in garnet (Fig. 7b, e), and inclusion trails in syn-deformational biotite (Fig. 7d). The direction of pressure shadows is parallel to the main biotite lineation of 145 to 155° dipping 20°-30° to SE for both samples. Pressure shadows comprise biotite, quartz, chlorite, white mica and plagioclase. S2 is strongly developed in the metapelitic domains, whereas in quartzofeldspathic ones, still relatively rich in mica, the foliation is more spaced. In the quartzofeldspathic domains only minor S-C structures and pressure shadows around porphyroclasts are developed. The D3 deformation is associated with minor horizontal crenulation folds with axes trending ~130 – 310°, developed mostly around porphyroclasts in the micaceous layers.

Garnet in both samples is euhedral to subhedral porphyroclasts with textural zonation. Quartz and ilmenite sigmoidal inclusion trails define S1. The trails direction in garnet cores varies across the samples, whilst in the rim they are frequently rotated syndeformationally with D1 (Figs 7a, e; 8a, b). Preservation of garnet blasts varies depending on the sample. In sample PSD03 garnet rims are rarely replaced by chlorite, while in sample PSB03 garnet is commonly nearly completely replaced by chlorite. Chemical profiles and maps of the garnet in PSD03 reveal the decrease of spessartine towards the rim (from 0.17 to 0.01), concomitant with the increase of almandine mole fraction (from 0.62 to 0.83). In the core, the grossular and pyrope mole fractions vary in the range of 0.17 – 0.20 and 0.02 – 0.03, respectively (Figs 8a, b; 9a-d). The Grossular mole fraction decreases to 0.10 in the outermost rim and the pyrope increases up to 0.10. The X_{Fe} ($X_{Fe} = Fe^{2+}/(Mg + Fe^{2+})$) decreases from the core towards the rim from 0.96 to 0.93 (Fig. 8a, b).

Biotite occurs in three microstructural positions: (a) biotite-I as porphyroclasts parallel to S1 (Figs 7 a; 10a); (b) biotite-II as blasts within S2 (Fig. 7b, d); and (c) blasts

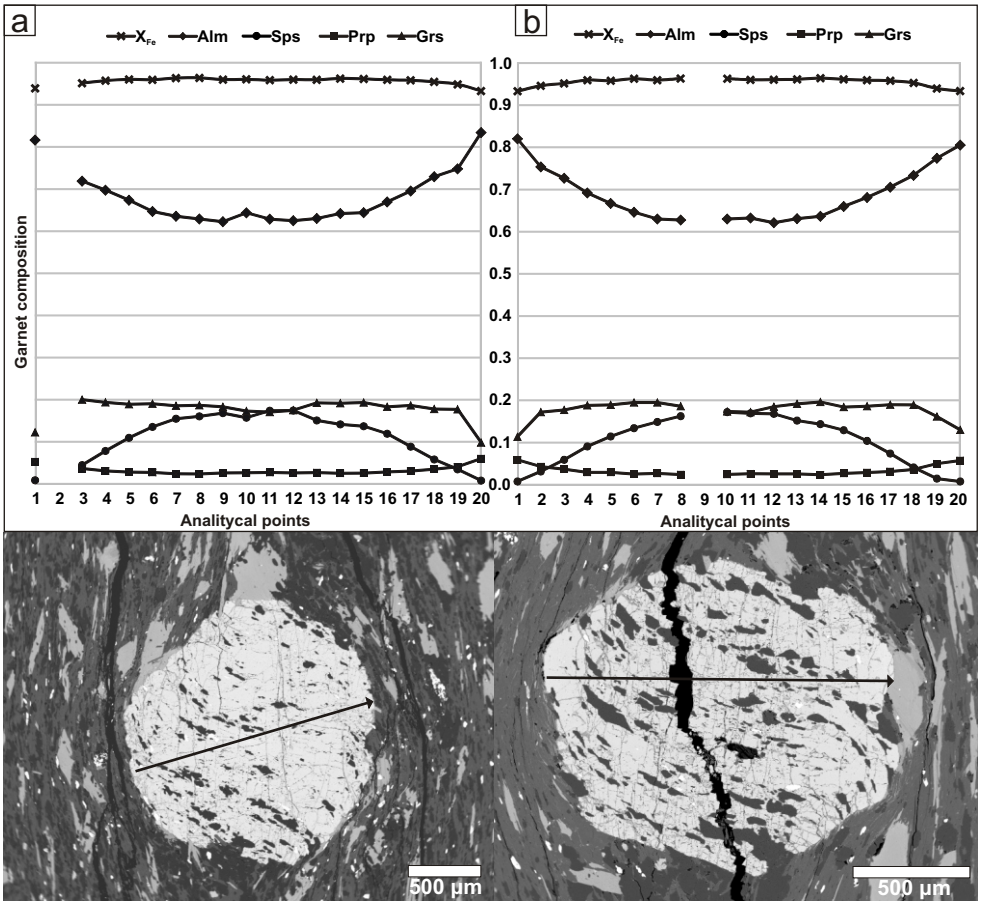

Figure 8. (a,b) Chemical composition of garnets in profiles. Almandine content increases at the expense of spessartine from core to rim. Grossular content decreases in the outermost rim where inclusion trails are bent.

in garnet pressure shadows. Biotite-I is characterized by a quartz inclusion-rich core and inclusion-poor rim. Biotite-II forms small (<0.5 mm) porphyroblasts (Fig. 7d) and blasts with tiny (<10 µm) inclusions trails aligning with S2 or slightly sinistrally rotated. Biotite in all structural positions is partially altered to chlorite in its outer parts and along internal cracks. Biotite-I is characterized by X_{Fe} ($X_{Fe} = Fe^{2+}/(Mg + Fe^{2+})$) of 0.63 – 0.65, Ti atoms per formula unite (a.p.f.u.) ranging from 0.10 to 0.12 and the Al^{VI} of 0.42 – 0.44 a.p.f.u. Biotite-II has similar X_{Fe} of 0.65 – 0.66 with slightly lower Ti of 0.07 – 0.08 a.p.f.u. and higher Al^{VI} substitution of 0.46 – 0.47 a.p.f.u. than biotite-I.

Muscovite forms small (<0.1 mm) flakes that highlight S1 and S2 and blasts of variable size in garnet pressure shadows (Fig. 7b). Muscovite-I in the matrix domains that still preserve S1 foliation and muscovite in the pressure shadows reveal higher Si of 3.13 – 3.18 a.p.f.u. than muscovite-II in the S2 foliation with Si of 3.09 – 3.10 a.p.f.u. Notably muscovite-I has a higher Mg of 0.11 – 0.14 a.p.f.u. and lower Al of 2.59 – 2.68 a.p.f.u. than muscovite-II with values of 0.07 – 0.08 a.p.f.u. and 2.74 – 2.77 a.p.f.u., respectively. Ti content is for all muscovite lower than 0.02 a.p.f.u.

Plagioclase forms relatively small (<0.2 mm) blasts aligned with S2 (Fig. 6a, b). Most of the bigger blasts are characterized by chemical zonation apparent on the Ca chemical map of garnet (Fig. 8d). The core is nearly pure albite with X_{Ab} (X_{Ab} = Na/(Na+Ca+K)) = 0.99 – 1.00 and the rim is more anorthitic with X_{Ab} = 0.91 – 0.92. The plagioclase is rarely affected by sericitization.

Ilmenite forms small (<0.1 mm) inclusions within garnet that are aligned with the S1 foliation (ilmenite-I) and as blasts within S2 (ilmenite-II). Ilmenite-I has higher pirophanite ($MnTiO_3$) content X_{Mn} (X_{Mn} = Mn/(Mn+Fe^{2+})) in the range of 0.03 – 0.05 than ilmenite-II with X_{Mn} in the range of 0.01 – 0.03.

Chlorite in both samples is replacing garnet and biotite in the outer parts and along fractures parallel to S2 and forms blasts in the garnet pressure shadows (Fig. 7b, e). In sample PSB03 chlorite forms pseudomorphs after garnet but only locally replaces biotite. Chlorite in strain shadows in the sample PSD03 has a chemical composition of chamosite with Mg of ~1.6 a.p.f.u.

Allanite forms aggregates included in biotite-I and garnet as well as dispersed in the matrix in both samples (Fig. 7b). Allanite belongs to the prograde M1 paragenesis as S2 wraps around the aggregates developing mainly quartz-filled pressure shadows indicating a sinistral sense of shear. Allanite is replaced by monazite, bastnäsite and epidote (Fig. 10b-d, f). Allanite is classified as allanite-(Ce) with homogenous composition character-

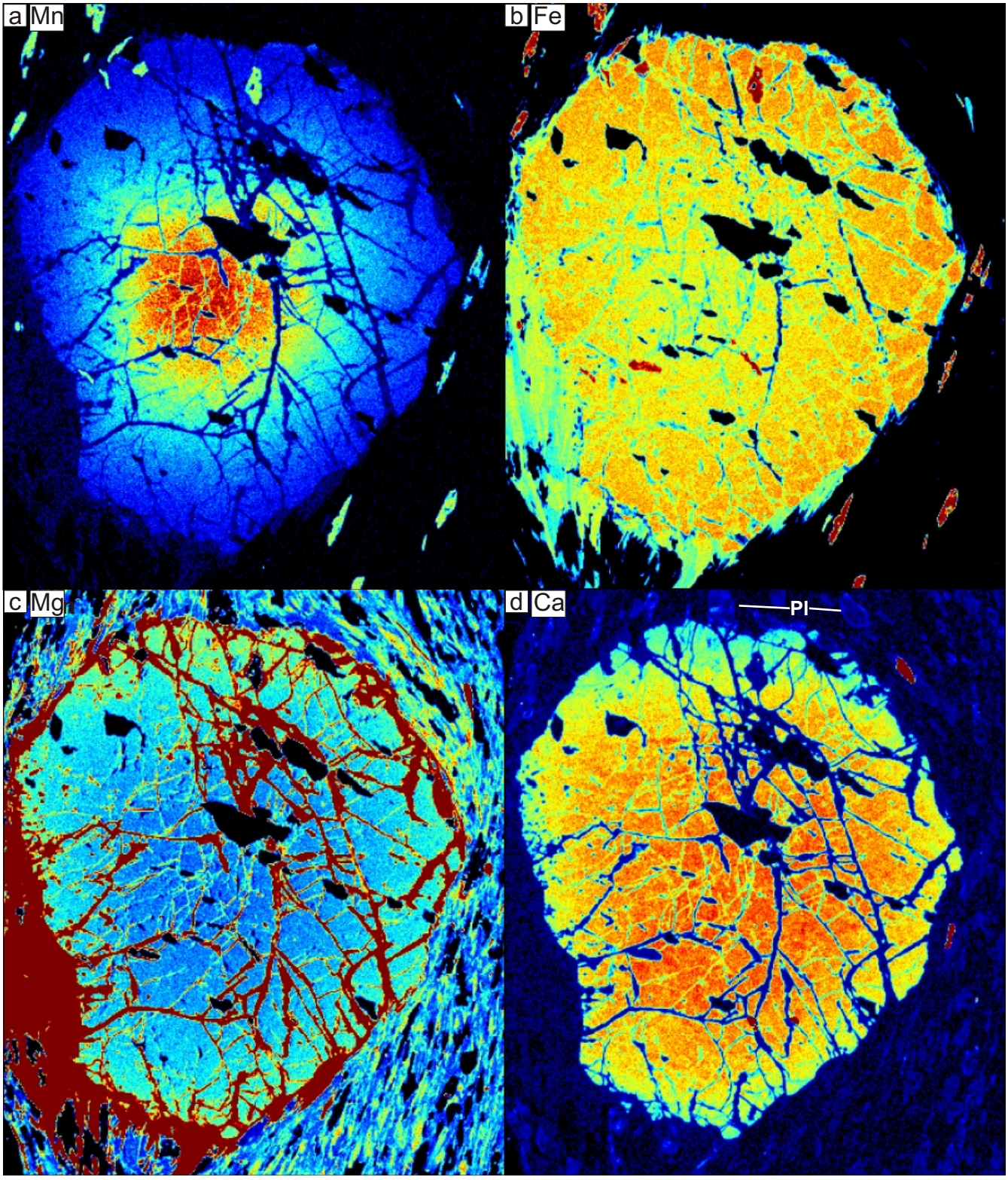

Figure 9. Electron microprobe X-ray chemical maps of garnet in sample PSDO3 with warmer colours indicating a higher concentration of elements: (a) Mn, (b) Fe content is increasing towards the rim in the expense of Mn content. (c) Mg content is increasing in the outermost rim. (d) Homogenous Ca content in the core is decreasing in the rim. Surrounding plagioclase blasts show increased Ca content in the rims. The base of the map is 0.5 mm wide.

ized by Ce of 0.42 – 0.43 a.p.f.u., La of 0.19 – 0.21 a.p.f.u. and Nd of 0.13 – 0.16 a.p.f.u.

Bastnäsite-(Ce) forms small (<20 μm) grains and surrounds or replaces allanite-(Ce) aggregates (Fig. 10f). It is characterized by Ce of 3.16 – 3.47 a.p.f.u., La of 1.76 – 1.80 a.p.f.u. and Nd of 1.35 – 1.55 a.p.f.u. resembling Ce to La to Nd ratios of allanite-(Ce).

Apatite occurs as blasts of variable size included in garnet and biotite-I and as blasts dispersed in the matrix. Rarely monazite coronas are developed around apatite in the matrix.

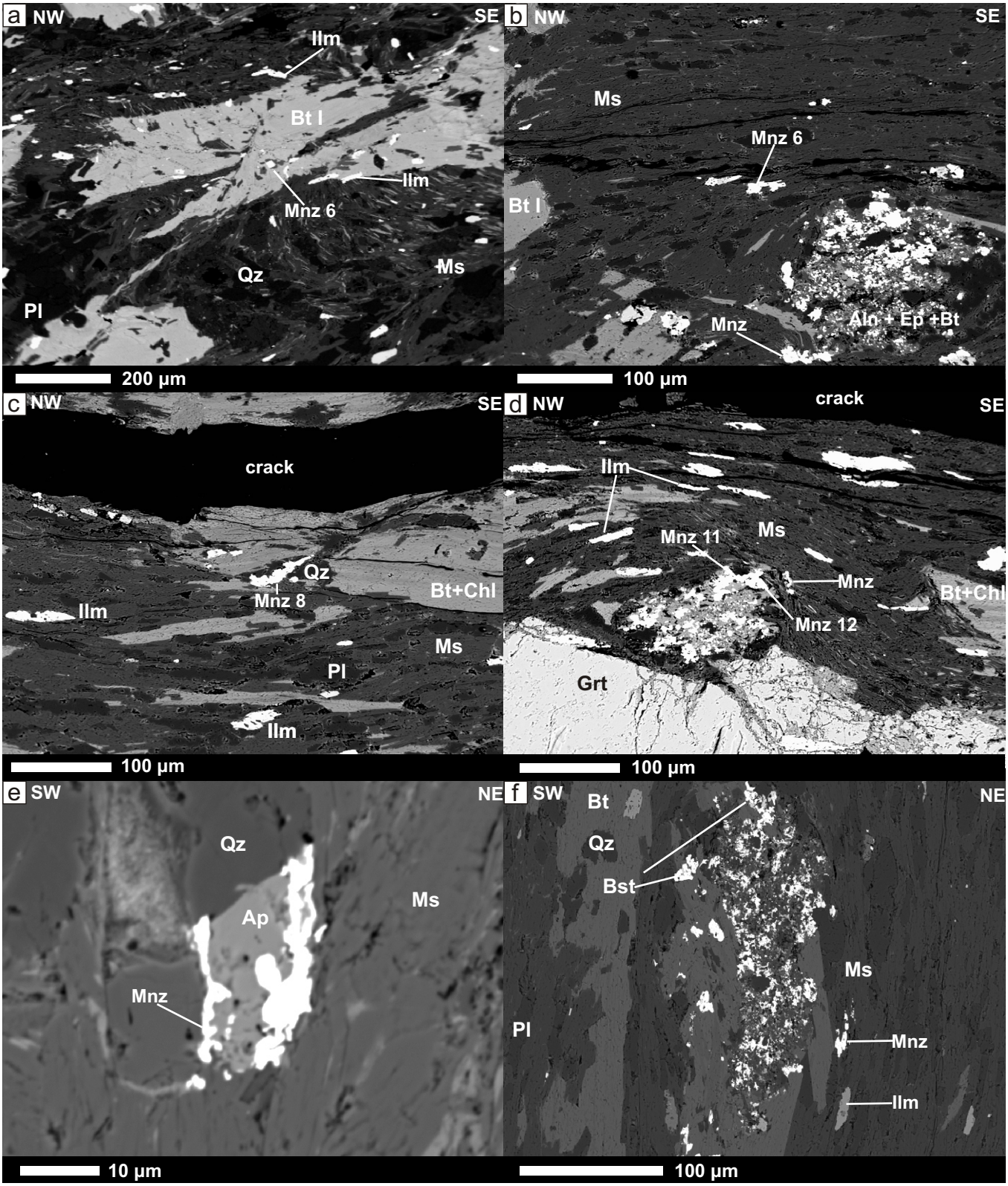

Figure 10. BSE images of REE-bearing phases: (a) Monazite-(Ce) within S2 foliation plane near allanite-(Ce) aggregate. Note asymmetric pressure shadow of the aggregate. (b) Monazite-(Ce) growing in expense of allanite-(Ce). (c) Monazite-(Ce) within a shear band developed in biotite. Biotite is being replaced by chlorite. (d) Satellite monazite-(Ce) surrounding allanite-(Ce) aggregate. monazite-(Ce) is forming along S2 foliation, that wraps around the aggregate. (e) Monazite-(Ce) corona on apatite. (f) Allanite-(Ce) in biotite blast surrounded by satellite bastänsite and monazite-(Ce) that is growing within S2 foliation plane.

4.3. Monazite-(Ce) chemistry and geochronology

Monazite-(Ce) forms blasts up to 20 µm in diameter. Several grains have been found in the biotite-I but not in the garnet and therefore they may represent a part of an early prograde M1 paragenesis or inherited grains for the sample PSB03 (Fig. 10a). Most of the remaining blasts unequivocally belong to M2 and are present in contact with allanite-(Ce) aggregates and in their close proximity. Several grains were found in the S2 foliation planes, C planes of S-C structures and single grain overgrowing a blast of apatite (Fig. 10b-e). Both monazite-

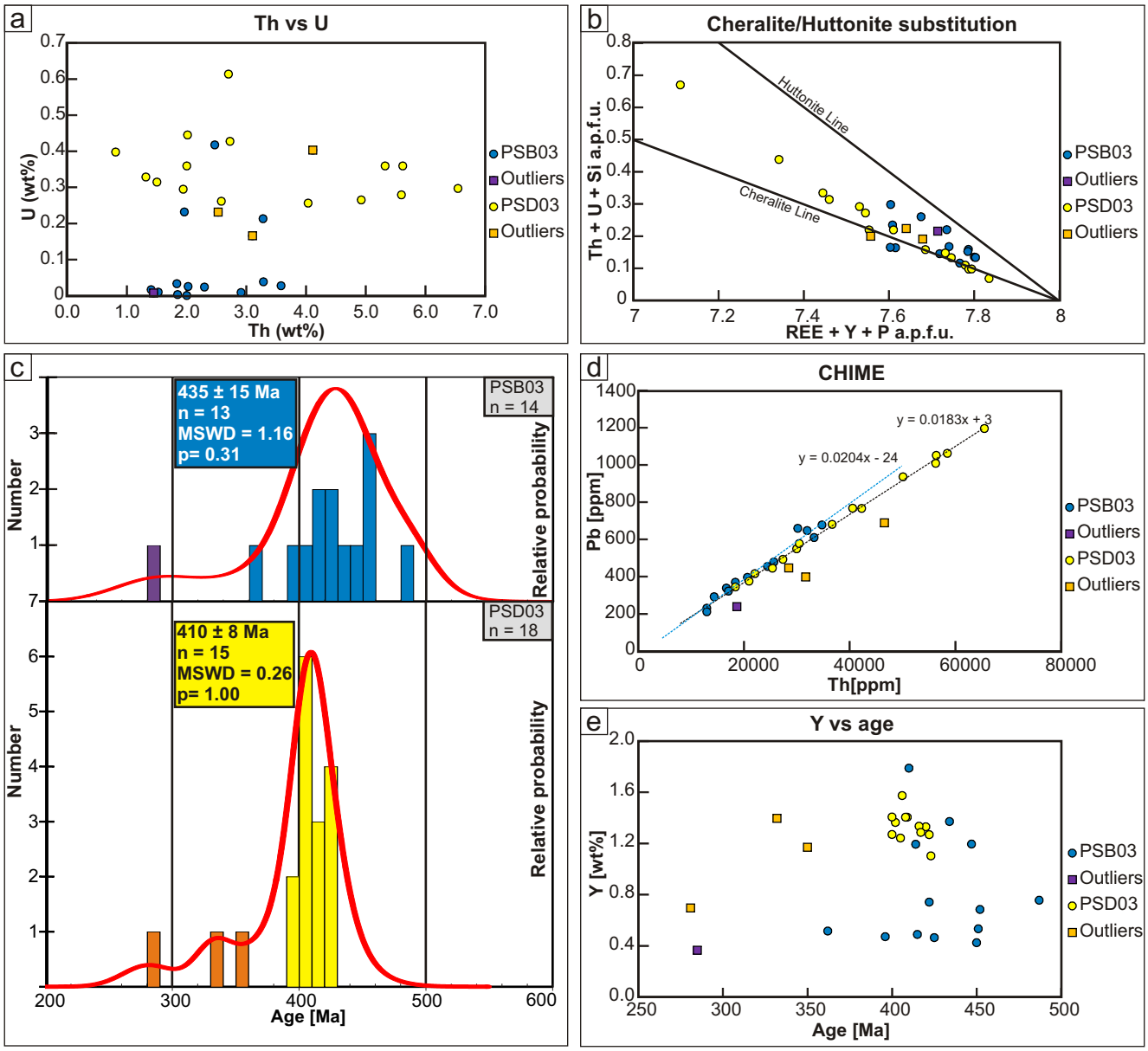

Figure 11. Chemical and geochronological characteristic of monazite-(Ce) for samples PSB03 and PSD03. (a) Th vs U plot of analyzed monazite-(Ce). (b) Monazite-(Ce) Th + U +Si vs. REE + P + Y substitution diagram. (c) Cumulative probability plots, with histograms, of monazite-(Ce) model dates. (d) Th* vs Pb isochron diagram after Suzuki et al. (1991). (e) Y vs monazite-(Ce) model dates diagram highlighting the uniform characteristics of monazite-(Ce) in sample PSD03.

(Ce) structural position and its replacement relationships to allanite-(Ce) suggest that monazite-(Ce) was formed in sample PSD03 during the M2 event. Its relation to bastnäsite-(Ce) remains enigmatic, as no clear contacts between these two minerals were found. Chemical analyses and Th-U-total Pb age determinations are presented in Tables S1 and S2.

Monazite-(Ce) in sample PSB03 has U content lower than 0.01 a.p.f.u. (<0.45 wt%) and Th content below 0.13 a.p.f.u. (3.5 wt%) (Fig 11a). Yttrium content differs in the range of 0.03 – 0.15 a.p.f.u. (0.4 – 1.8 wt%) and displays higher variability than in sample PSD03. Cheralite and huttonite substitutions in all analyzed monazite-(Ce) display low variability with values within the range of 0.03 – 0.07 (Fig. 11b).

Monazite-(Ce) chemical composition in the sample PSD03 is homogenous. Uranium content is lower than 0.02 a.p.f.u. (<0.55 wt%) and Y is in the range of 0.06 – 0.13 a.p.f.u. (0.5 – 1.1 wt%) with most analyses (n = 17/18) in the range of 0.10 – 0.13 a.p.f.u. The main variable in composition are Th content ranging from 0.03 to 0.23 a.p.f.u. (0.7 – 6.0 wt%) and Ca content of 0.05 – 0.19 a.p.f.u. (0.2 – 0.8 wt%). This two-element correlative variation, accounting for cheralite substitution, results in concomitant variations in the remaining elements in cationic positions.

Th-U-total Pb single spot model dates (n = 14) were collected from 10 grains in the sample PSB03, from both structural positions i.e. inclusions in biotite porphyroblasts and in the matrix, and yielded an array of ages 487 – 285 Ma (Fig. 11c). Weighted average of all dates

gives 428 ± 25 Ma with MSWD = 2.7 and p = 0.001. Excluding the youngest single date (285 Ma, which does not overlap with the weighted average of the whole population), the weighted average is 435 ± 15 Ma with MSWD = 1.16 and p = 0.31. The equivalent sum of Th and U content (Th*) shows a lower spread in comparison with monazite-(Ce) from sample PSD03, resulting in a higher error of obtained single model dates. The intercept of the isochron ages corresponds to an estimated Pb-loss of 24 ppm Pb (± 60 ppm) (Fig. 11d). No correlation between the chemical composition, structural position, and obtained model dates was found (Fig. 11e).

Th-U-total Pb single spot model dates (n = 18) were collected from 14 analyzed blasts in the sample PSD03. The dates form a cluster in the range of 390 – 430 Ma with three distinctively younger dates of 350 ± 45 Ma, 332 ± 28 Ma and 281 ± 40 Ma that do not overlap with the cluster weighted average (Fig. 11c). Calculation of all model dates in the cluster yielded a weighted average of 410 ± 8 Ma with MSWD = 0.26, and p = 1.00 (Fig. 11c). High probability with low MSWD, consistent chemical composition and structural position of monazite-(Ce) indicate that it belongs to only one population. Statistical analysis of the chemical Th-U-total Pb dates using isochron diagrams of Suzuki et al. (1991) yielded an intercept corresponding to a negligible amount of common Pb – 3 ppm (± 15 ppm) or insignificant Pb-loss (Fig. 11d).

4.4. Conventional geothermobarometry

Pressure - temperature (P-T) estimates were performed using the Holdaway (2001) garnet-biotite geothermometer and the geobarometer of Wu (2019) – Ca-Fe in garnet exchange geobarometry. For the early prograde stage, garnet and biotite-I cores were used, while peak temperature conditions were estimated using garnet and biotite-I rims (Table S3). Plagioclase-based geobarometers could not be applied as plagioclase in the studied rocks is Ca-deficient. P-T estimates for sample PSD03 based on the nine pairs of garnet-biotite-I cores suggest equilibration at 6.6 – 7.1 kbar at 480 – 520°C, while 15 pairs of garnet-biotite-I rims yielded conditions of 5.1 – 5.9 kbar and 530 – 560°C, which represent peak temperature conditions.

5. Discussion

5.1. Metamorphic evolution

The mineral assemblage M1, preserved mainly as porphyroclasts in sample PSD03, and microdomains in sample PSB03, reached a garnet zone of lower amphibolite facies with no evidence of staurolite growth. The lack of staurolite may be related to the original bulk chemistry of the rock, nevertheless the high mica content in the rock and rare occurrences of epidote-zoisite group minerals suggest a low-Ca and high-Al bulk composition. A record of an early prograde metamorphic event, up to peak pressure conditions, is preserved in the garnet core. Decreasing spessartine mole fraction and X_{Fe} ratio is typical for upper greenschist – lower amphibolite facies (e.g. Tracy et al. 1976). P-T conditions of the garnet core equilibration are 6.6 – 7.1 kbar at 480 – 520°C. The higher pyrophanite content in the ilmenite inclusions enclosed in the garnet than those in the matrix confirms that the garnet was not overgrowing pre-existing fabric (Hollister 1966; Palin et al. 2015). In the garnet core and in biotite-I blasts the inclusion trails show no signs of rotation. Plagioclase at this stage was represented by pure albite.

The further prograde metamorphic stage is recorded within the garnet rim and plagioclase rims. Decreasing grossular content in the garnet rim corresponds to the increase of anorthitic content in plagioclase. No apparent change in spessartine or X_{Fe} trend occurs between the core and rim, suggesting growth of garnet via continuous reaction at this stage. Concurrently, the inclusion trails in the garnet rim show a rotational trend indicating either left-lateral (sample PSD03) or right-lateral (sample PSB03) shearing. This stage of prograde metamorphism was most probably associated with the garnet growth between peak pressure and peak temperature, as the garnet shows the decrease of the X_{Fe} in the rim characteristic of prograde growth (Fig. 8a, b). Observed paragenesis muscovite + quartz + biotite + plagioclase + garnet + ilmenite + allanite-(Ce) agrees with peak metamorphic conditions estimates of 5.1 – 5.9 kbar at 530 - 560°C similar to 6.6 kbar at 535°C provided by Ague, Morris (1985). Minor pressure disparity between these results may be related to different geobarometric method calibrations used or better preserved garnet rim in the analyzed samples. Allanite-(Ce) aggregates included in biotite-I as well as garnet core and rim attest that the rock did not reach the monazite-(Ce)-in isograd during amphibolite facies prograde stage (e.g. Spear 2010). Therefore, the monazite-(Ce) included in biotite-I in the sample PSB03 most probably represents an early prograde monazite-(Ce) (i.e. lower greenschist facies; e.g. Wing et al. 2003) growth preserved through the peak prograde stage. Alternatively, such lower greenschist facies monazite-(Ce) was dissolved and reprecipitated, which resulted in precursor-related Pb inheritance in microdomains (Seydoux-Guillaume et al. 2018). The lack of monazite-(Ce) in the garnet in all samples supports that hypothesis. The temperature conditions of monazite-(Ce)-in isograd are highly dependent on the Ca content or Ca/Na content ratio in the rock, but even in the low-Ca metapelites the partial allanite-(Ce) break-

down to monazite-(Ce) occurs at ~560 – 570°C (e.g. Foster, Parrish 2003; Janots et al. 2008). No evidence of amphibolite facies monazite-(Ce) was found, thus the obtained P-T conditions, although representing a rough estimate of garnet rim equilibration, are in agreement with previous research. In this study the bulk rock composition was not analyzed, therefore providing further constraints on the monazite-(Ce)-in isograd is impossible.

The M2 metamorphism occurred under the greenschist facies conditions and was associated with the development of S2 obliterating structures developed during M1. In the more competent micaceous domains the grain size was reduced and all of the white mica and plagioclase as well as the majority of the biotite does not exceed 100 μm. The nearly homogenous composition of biotite-I and -II in deformed domains suggests that during M2 biotite-I blasts were recrystallized. Biotite-II, forming blasts rotated with a sinistral sense of shear, was stable during the early M2. However, biotite-I and garnet are decomposing to chlorite along fractures parallel to S2, which suggests that fluid-associated retrogression could be driven below the biotite zone of greenschist facies. Alternatively, the increased fluid flow along S2 resulted in the change of local H_2O gradients that allowed chlorite formation on the garnet-biotite boundaries (e.g. Tursi 2022). However, the pressure shadow assemblage includes biotite-II with Ti and Al^{IV} contents lower than their counterparts in the matrix, thus registering the drop in temperature and pressure (e.g. Henry, Guidotti 2002). Additionally, higher Al and low Ti content in muscovite-II in the matrix suggest that it has recrystallized under greenschist facies conditions (Guidotti, Sassi 1986; Mulch, Cosca 2004).

Allanite-(Ce) aggregates were partly replaced by monazite-(Ce) during M2, forming "satellite" blasts around them and single blasts aligned with S2. Monazite-(Ce) in the sample PSD03 has a relatively higher Y content than its precursor allanite-(Ce). Therefore, this enrichment has to be originated either from fluid or from decomposing garnet - the main Y sink in metapelites (Yang, Pattison 2006). The monazite-(Ce) growth should be attributed to the allanite-(Ce) to monazite-(Ce) retrogressive transition that was documented for metamorphic temperature conditions of about 450°C (Janots et al. 2006, 2008; Krenn, Finger 2007; Palin et al. 2015; Wing et al. 2003). With the presence of F- and CO_2-rich fluids, the retrograde bastnäsite-(Ce) forming reaction can occur at similar temperatures (Savko, Bazikov 2011). The structural position of bastnäsite-(Ce) blasts occurring only around allanite-(Ce) aggregates and not in S2 suggests that it was formed at the expense of allanite-(Ce) and not monazite-(Ce). The discrepancy between the bastnäsite-(Ce) and monazite-(Ce) structural positions may be related to the growth of the former after the main phase of shearing. The relaxation phase would then provide the pathways for fluids carrying elements necessary to aid the allanite-(Ce) - bastnäsite-(Ce) transition. Alternatively, bastnäsite-(Ce) may be entirely related to a much later, low-temperature alteration.

5.2. Interpretation of monazite-(Ce) geochronology

Despite the monazite-(Ce) in the sample PSB03 being present in two structural positions, there is no apparent correlation between the obtained single model dates and monazite-(Ce) chemistry or its structural position. Biotite did not deliver sufficient shielding for monazite-(Ce) as the cleavage provided pathways for fluid infiltration related to M2, which resulted in altering a primary monazite-(Ce) composition. The significant spread of model dates as well as the observed variability in cheralite and huttonite substitutions her with U and Y content in the monazite-(Ce) from sample PSB03 suggests that its formation was related to multiple processes with local chemistry or composition of monazite-(Ce) precursor involved (e.g. Janots 2006; Wing et al. 2003). The weighted average age of 435 ± 15 Ma is therefore a mixed age between at least two different populations. Low Th* resulted in a high error on single model dates in sample PSB03 and did not allow us to separate the M2 monazite-(Ce) from older grains. An inherited detrital monazite-(Ce) component can be considered. However, the depositional age of the Müllerneset Formation is thought to be late Mesoproterozoic/Early Neoproterozoic, therefore the such origin of monazite-(Ce) would require a strong partial resetting of the U-Th-Pb system of monazite-(Ce) and most probably would result in an even greater spread of model dates. Monazite-(Ce) enclosed in biotite-I was likely formed at early stages of prograde metamorphism and was later partially reset or dissolved and reprecipitated during M2 event, which does not allow to constrain the timing of early (lower greenschist facies) prograde M1. Preservation of early prograde or inherited grains of monazite-(Ce) has been reported even up to higher amphibolite facies (e.g. Finger et al. 2016; Krenn et al. 2008; Wing et al. 2003). Nevertheless in the studied rock the preservation potential for an earlier generation was low due to the relatively small size of the grains (<20 μm) and following fluid-assisted retrograde shearing. Therefore the Ordovician-Silurian dates obtained here might not reflect a true early prograde (M1) metamorphic age.

The structural position of monazite-(Ce) in S2 foliation and replacing peak metamorphic allanite-(Ce) defines the age of 410 ± 8 Ma in the sample PSD03 as a constrain on the timing of the sinistral shearing during the retrogressive M2 event. In contrast to the sample PSB03,

monazite-(Ce) in sample PSD03 has uniform Y and U contents, whereas its chemical variability relates to the increasing cheralite substitution with the influence of huttonite substitution increasing for high-Th content (Fig. 11b). The Suzuki et al. (1991) isochron diagram defines an intercept corresponding to an insignificant amount of common Pb – 3 ppm (± 15 ppm) or minor Pb-loss, suggesting that the tight 410 ± 8 Ma cluster is devoid of inherited component and does not show signs of Pb-loss due to later tectonic events. Several younger model dates in both samples suggest that possible Pb-loss or partial resetting could occur during the brittle to ductile Eurekan event, similar to step heating $^{40}Ar/^{39}Ar$ white mica geochronology revealing argon-loss that was attributed to Paleogene deformation (Dallmeyer 1989). The difference between monazite-(Ce) ages in the samples highlights the observed increasing intensity of D2 shearing from the east (PSB03) to the west (PSD03) of western Svartfjellstranda. At the microscale it allowed for the preservation of monazite-(Ce) record from earlier, potentially Ordovician (ca. 450 Ma), event that is completely obliterated in the higher-strain zone to the West.

The obtained 410 ± 8 Ma age of retrogressive monazite-(Ce) growth in the Müllerneset Formation is identical to the reported 410 ± 2 Ma $^{40}Ar/^{39}Ar$ cooling age of white mica, which was lacking a microstructural context (Dallmeyer 1989). However, in the light of the observed behaviour of white mica it is possible to deduce that this age represents either dynamic neo-/re-crystallization or fast cooling after it. Identical age obtained for these two minerals suggests that the monazite-(Ce) formation and the muscovite neo-/re-crystallization in the greenschist facies conditions occurred basically contemporaneously, resembling the situation observed in the eastern Himalayan syntaxis (Palin et al. 2015).

The age relation between M1 and M2 cannot be assessed without geochronological data for the prograde metamorphism. The retrograde reaction continuum with dynamic recrystallization of micas in biotite grade, retrogressive monazite-(Ce) growth and chloritization of garnets may have been subsequent to prograde metamorphism in the garnet zone of lower amphibolite facies. However, the shift from right to left lateral motion recorded by rotation of some of the garnet inclusion trails to the left-lateral shearing during retrogression was most probably not instantaneous. The emplacement of post-D1 quartz veins that are subsequently rotated during D2 suggests that the deformation events were separated by a relaxation period of an unknown time span.

The Gipsdalen Group that is unconformably overlying the Müllerneset Formation suggests that the latter was exposed to the surface prior to mid-late Carboniferous. The retrogression in the Müllerneset Formation was likely caused by tectonically driven uplift. Structural observations indicate, assuming the lack of post-metamorphic reorientation, that the uplift took place through the sinistral, oblique-slip displacement in the NNW-SSE direction. More intense shearing in the Müllerneset Formation observed in the western Svartfjellstranda suggests that the main displacement occurred west of the present-day Spitsbergen shore.

5.3. Tectonic implications

5.3.1. Structural framework of the Müllerneset Formation

The Müllerneset Formation shows the opposite attitude of dipping of S2 in the western and eastern parts of Svartfjellstranda, which was interpreted as a younger anticline (Ague, Morris 1988). Blocks and lenses of Carboniferous rocks that are exposed on the prolongation of the axis of this anticline suggest that it is a younger structure that represents a projection of the western fault of the SEDL exposed farther south (Maher et al. 1997). Southwestwardly dipping Carboniferous rocks are in unconformable contact with the Müllerneset Formation in its easternmost outcrops (Figs 6a; 12). The contact is tectonized but suggests that eastern Svartfjellstranda represents a block reoriented during the early compressional stage of Eurekan deformation. Similar reorientation has been documented ~15 km south in the Eidembukta area (Fig. 1b), where southernmost exposures of the Müllerneset Formation in between the SEDL border faults and represent a core of an overturned anticline. The western fault of the SEDL is moderately westward dipping and characterized mainly by dip-slip structures moving farther north from the Eidembukta to the Svartfjella area (Maher et al. 1997). F3 mesoscale folds characterized by NE dipping axial planes and gently plunging axes trending NNW-SSE and NW-SE (Figs 3e; 5e, f) resemble the structures reported from the Eidembukta area. Field observations and regional correlations suggest that eastern Svartfjellstranda represents a similar part of an overturned anticline that is bounded by the SEDL border faults. Further reorientation during the transpressional-transtentional stage of Eurekan deformation might not allow precise reorientation of eastern Svartfjellstranda into pre-Eurekan position following the reorientation applied to rotated Caledonian structures of the Berzeliuseggene unit (Majka et al. 2014). Correlating S2 and the opposite sense of shear in eastern and western Svartfjellstranda, together with the overturned position of the unconformably overlying Carboniferous rocks, suggests that the clockwise rotation of the Müllerneset Formation in its eastern part

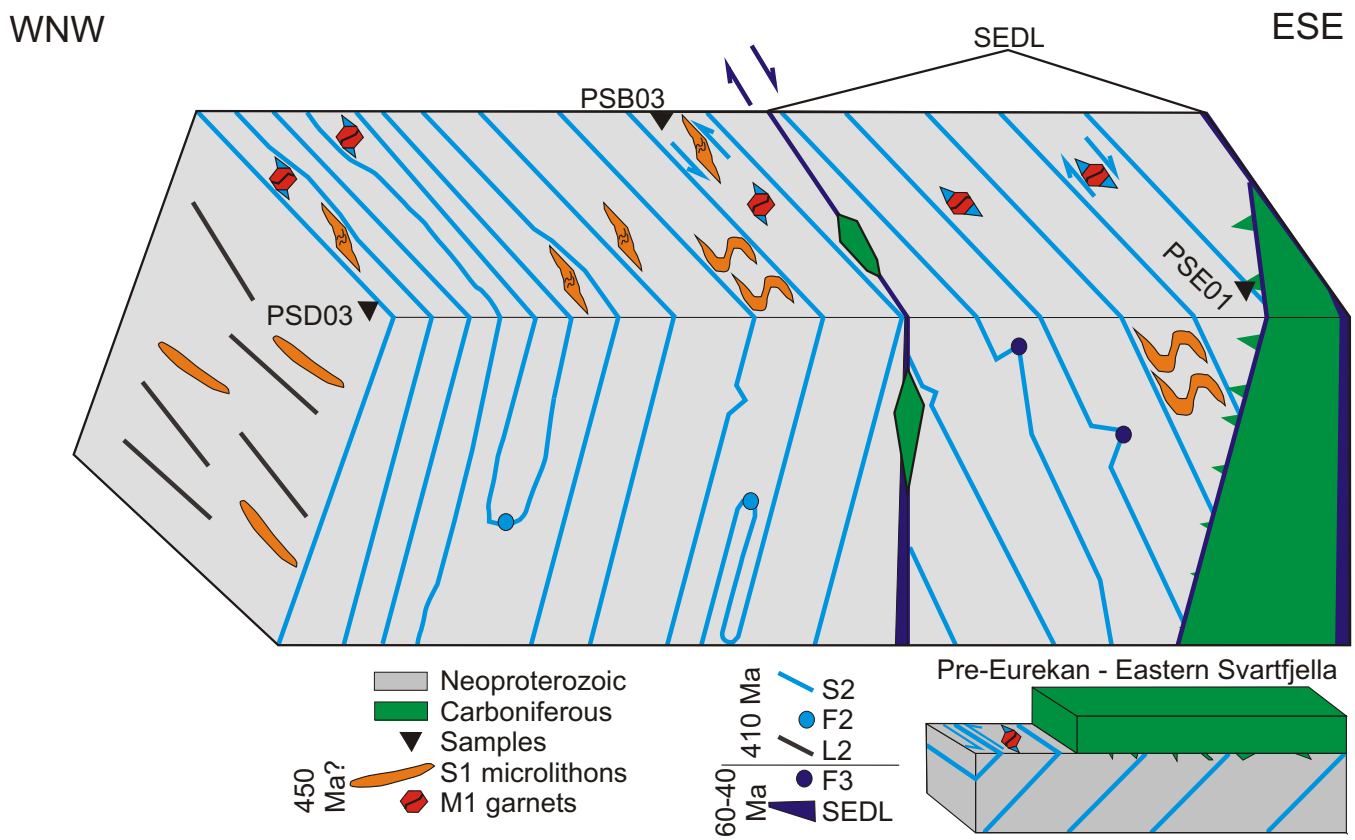

Figure 12. Schematic sketch across Svartfjellstranda with pre-Eurekan reorientation of the eastern Svartfjellstranda. In pre-Eurekan position apparent dextral sense of shear is reoriented into sinistral sense of shear. Note increasing shear gradient toward the westernmost outcrops.

was in the range of ~120° along NW-SE trending axes of F3 folds resulting in an overturned position of eastern Svartfjellstranda.

5.3.2. Relation to remaining Oscar II Land pre-Carboniferous Basement

The relationship between the Müllerneset Formation and the lithologies cropping out in the chaotic zone remains unclear as they are separated by the SEDL. Nevertheless, the deformation events can be correlated across the SEDL. D1 is associated with prograde M1 in the autochtonous basement of Oscar II Land (Michalski et al. 2014; Morris 1988). In the Müllerneset Formation the geodynamic framework of D1 cannot be assessed, but in the remaining Caledonian basement, it is characterized by nearly horizontal N-S trending isoclinal folds of undetermined vergence (Michalski et al. 2014; Morris 1988). The timing of D1 deformation in the basement of Oscar II Land predates the sedimentation of the Late Ordovician-early Silurian Bullbreen Group (Morris 1988). The early generation of monazite-(Ce) in the Müllerneset Formation might reflect the processes associated with the prograde M1 event in the remaining Oscar II Land basement. The D2 event in western Svartfjellstranda is characterized by NNW-SSE trending left-lateral shearing with gently SSE plunging (maximum at 162/18) stretching lineations. A similar structural trend is displayed by east vergent F2 axes in the eastern Oscar II Land basement and from Holmesletfjellet to Motalafjella, where the Vestgötabreen Complex and the Bullbreen Group are exposed in the overturned west vergent syncline (syncline axis dipping 12° to 158°) of inferred late Caledonian age (Labrousse et al. 2008; Michalski et al. 2014; Morris 1988). The D2 event should be related to greenschist facies overprint and E to ENE thrusting, post-dating northward thrusting in the Vestgötabreen Complex, and characterized by monazite-(Ce) ages of ca. 430 Ma and 410-395 Ma obtained using Th-U-total Pb method (Barnes et al. 2020).

Parallelism of both strike-slip and compressional ca. 410 Ma late-Silurian-Early Devonian structures in the Oscar II Land basement suggests that they formed in the transpressional regime, where the strain has been partitioned into several domains. The Svartfjellstranda area is dominated by the left-lateral strike to oblique slip that resulted in the uplift of the Müllerneset Formation. In the transitional so-called 'chaotic zone' to the east, the NNW-SSE trend of Silurian-Devonian structures continues, however strong influence of Eurekan deformation resulted in refolding earlier structures into apparent westward vergence (Braathen et al. 1999; Manby 2014). Farther west Oscar II Land basement is dominated by ENE-directed thrusting and folding (Michalski et al. 2014; Morris 1988). Transitional zones between these domains are not exposed and spatial trends characterizing both stages of the Eurekan deformation are simi-

lar to the observed Silurian-Early Devonian structures, therefore brittle rejuvenation of the latter by the former is common (e.g. Piepjohn et al. 2016). Generalizing the observed structural patterns in the basement of Oscar II Land suggests an oblique convergence in NW-SE or WNW-ESE (present-day coordinates) in the Early Devonian.

5.3.3. Implications for structural development of the Southwestern Basement Province

The recorded NNW-SSE trending left-lateral high-strain zone in the amphibolite facies Müllerneset Formation poses a question about what was the block that it was juxtaposed against in the Early Devonian. The PKF pre-Ellesmerian basement separated from Spitsbergen by the Forlandsundet Graben (e.g. Tyrell 1924) seems to be the most likely candidate to represent the crustal fragment juxtaposed against the Müllerneset Formation. Structural development of the PKF pre-Ellesmerian basement consists of D1 associated with prograde M1 followed by D2 characterized by NNW-SSE to NW-SE trending isoclinal folds with west-southwest vergence (Manby 1986; Piepjohn et al. 2000). No age constrains on pre-Ellesmerian structures in PKF are available so far, however the age of D2 was inferred to be Caledonian (Piepjohn et al. 2000). The structures in Oscar II Land and PKF although of opposite vergence have been discussed as potentially coeval (Manby 1986) and formed during the same transpressional event. There is no geochronological information about the timing of deformation in PKF, therefore it might be unrelated to the deformation in Oscar II Land. However, if they are in fact coeval and formed in a transpressional regime most probable explanation is that they form opposite wings of the positive flower-structure on the restraining bend of the major shear zone.

Tectonic slivers of the Vestgötabreen Complex and the Bullbreen Group exposed in the tectonized zone in Sarsøyra of northern Oscar II Land (e.g. Ohta et al. 1995; Scrutton et al. 1976) may mark the northern continuation of the high-strain zone exposed in Svartfjellstranda. The southern continuation may be exposed in the Wedel Jarlsberg Land, where the Tonian Berzeliuseggene unit, metamorphosed in amphibolite facies in the late Neoproterozoic and under HP conditions in the Ordovician, is juxtaposed against low-grade Neoproterozoic metasediments along a similar NNW-SSE trending sinistral shear zone dated to 410 ± 18 Ma (Faehnrich et al. 2020; Majka et al. 2015). In contrast to Oscar II Land, the HP unit is exposed on the western side of the coeval left-lateral shear zone (Majka et al. 2015). The projection of these two NNW-SSE trending shear zones would connect in Nordenskiöld Land, where equivalents of the Vestgötabreen Complex were documented (Kośmińska et al. 2014). The observed dismemberment of Ordovician HP units along the western coast of Spitsbergen confirms the claim that the complexity of the SBP is related to the activity of an Early Devonian sinistral shear zone or a set of anastomosing shear zones (Mazur et al. 2009; Majka et al. 2015; Faehnrich et al. 2020).

Documented in Oscar II Land transpression expressed in zones of NNW-SSE sinistral strike and ENE-WSW shortening resembles structures that are characteristic translational dismemberment of the terrane along continental margin subsequent to its oblique accretion (e.g. Coney et al. 1980). High-strain zone in Svartfjellstranda might be linked to the inferred structures related to the translation of the Pearya Terrane along the Franklinian Basin of northern Laurentia in the Ordovician to Devonian (Gosen et al. 2012; Kośmińska et al. 2022; McClelland et al. 2021; Trettin 1987). Alternatively, the transpressional event in Oscar II Land can be correlated with structures attributed to the proposed Caledonian escape tectonic observed in Ny Friesland (Gee, Page 1994; Lyberis, Manby 1999). The timing of the postulated lateral escape varies from ca. 431 – 428 Ma in the Scandinavian Caledonides (Kirkland et al. 2006) to ca. 350 Ma in the Greenland Caledonides (Hallett et al. 2014) and overlaps with the activity of the CATS. Whether the Southwestern Basement Province of Svalbard was assembled by one of these systems of transcurrent faults acting alone or represents an interaction between the two systems requires further research.

6. Conclusions

The Müllerneset Formation experienced lower amphibolite facies metamorphism (M1) followed by retrogressive greenschist facies event (M2) associated with NNW-SSE trending left-lateral to oblique shearing. The timing of the prograde event could not be precisely determined, but it is most probably Ordovician (ca. 450 Ma). Still, the retrogressive event associated with the second generation of monazite-(Ce) growth is dated to 410 ± 8 Ma. Decreasing pressure-temperature conditions of M2 and unconformable contact overlying Gipsdalen Group suggest that the Müllerneset Formation experienced fast tectonic exhumation starting in Early Devonian and finished before mid-Carboniferous. Coeval greenschist facies metamorphism in the Oscar II Land Basement east of SEDL (Barnes et al. 2020) was related to WSW-ENE shortening and development of east vergent folds as well as eastward thrusting. The nearly perpendicular direction of contraction and left-lateral shearing suggest that these deformations were related to the Early Devonian transpressional regime in the area. Sinistral strike to oblique-slip documented in the western Oscar II Land

is another evidence for the existence of an anastomosing set of Silurian-Early Devonian shear zones developed in the Southwestern Basement Province (Faehnrich et al. 2020; Majka et al. 2015). These shear zones resulted in the transpressional displacement of Neoproterozoic metasediments and Ordovician HP complex in the form of a tectonic block(s) along the western coast of Spitsbergen, creating a complex internal structure of the Southwestern Basement Province.

Acknowledgements

This study was supported by the National Science Centre (Poland) research project 2015/17/B/ST10/03114 awarded to J. Majka, Research Council of Norway Arctic Field Grant no. 282546 awarded to GZ and AGH statutory funds 16.16.140.315. We thank all participants of the 2017 and 2018 field seasons, with special thanks to Paweł Słupski for help with sample collection. We are grateful to Polish Polar Station in Hornsund and Nicolaus Copernicus University Polar Station in Kaffiøyra, as well as crews of Eltanin and Ocean A for logistical support. Adam Włodek, Gabriela Kozub-Budzyń, and Patrik Konečný are acknowledged for their help with EMP analyses. William C. McClelland and the anonymous reviewer are thanked for their constructive reviews that helped to improve the manuscript. Silvio Ferrero is acknowledged for editorial handling.

Conflicts of interest

The authors have no conflicts of interest to declare.

Supplementary Material

Supplementary data to this article can be found online at https://doi.org/10.2478/mipo-2022-0007.

References

Ague, J. J., & Morris, A. P. (1985). Metamorphism of the Mullerneset Formation, St. Jonsfjorden, Svalbard. *Polar Research, 3*(1), 93-106. DOI: 10.3402/polar.v3i1.6941.

Barnes, C. J., Walczak, K., Janots, E., Schneider, D., & Majka, J. (2020). Timing of Paleozoic Exhumation and Deformation of the High-Pressure Vestgötabreen Complex at the Motalafjella Nunatak, Svalbard. *Minerals, 10*(2), 125. DOI: 10.3390/min10020125.

Bazarnik, J., Majka, J., McClelland, W. C., Strauss, J. V., Kośmińska, K., Piepjohn, K., Elvevold, S., Czupyt, Z., & Mikuš, T. (2019). U-Pb zircon dating of metaigneous rocks from the Nordbreen Nappe of Svalbard's Ny-Friesland suggests their affinity to Northeast Greenland. *Terra Nova, 31*(6), 518-526. DOI: 10.1111/ter.12422.

Braathen, A., Bergh, S. G., & Maher Jr, H. D. (1999). Application of a critical wedge taper model to the Tertiary transpressional fold-thrust belt on Spitsbergen, Svalbard. *Geological Society of America Bulletin, 111*(10), 1468-1485. DOI: 10.1130/0016-7606(1999)111<1468:AOACWT>2.3.CO;2.

Dallmann, W. K. (2015). *Geoscience atlas of Svalbard*. Tromsø: Norsk Polarinstitutt.

Dallmeyer, R. D. (1989). Partial thermal resetting of $^{40}Ar/^{39}Ar$ mineral ages in western Spitsbergen, Svalbard: possible evidence for Tertiary metamorphism. *Geological Magazine, 126*(5), 587-593. DOI: 10.1017/S001675680002286X.

Dineley, D. L. (1958). A review of the Carboniferous and Permian rocks of the west coast of Vestspitsbergen. *Norsk Geologisk Tidsskrift, 38*, 197-217.

Elvevold, S., Ravna, E. J., Nasipuri, P., & Labrousse, L. (2014). Calculated phase equilibria for phengite-bearing eclogites from NW Spitsbergen, Svalbard Caledonides. *Geological Society, London, Special Publications*, *390*(1), 385-401. DOI: 10.1144/SP390.4.

Engi, M. (2017). Petrochronology based on REE-minerals: monazite, allanite, xenotime, apatite. *Reviews in Mineralogy and Geochemistry*, *83*(1), 365-418. DOI: 10.2138/rmg.2017.83.12.

Faehnrich, K., Majka, J., Schneider, D., Mazur, S., Manecki, M., Ziemniak, G., Wala, V. T., & Strauss, J. V. (2020). Geochronological constraints on Caledonian strike-slip displacement in Svalbard, with implications for the evolution of the Arctic. *Terra Nova, 32*(4), 290-299. DOI: 10.1111/ter.12461.

Finger, F., Broska, I., Haunschmid, B., Hrasko, L., Kohút, M., Krenn, E., & Uher, P. (2003). Electron-microprobe dating of monazites from Western Carpathian basement granitoids: plutonic evidence for an important Permian rifting event subsequent to Variscan crustal anatexis. *International Journal of Earth Sciences*, *92*(1), 86-98. DOI: 10.1007/s00531-002-0300-0.

Finger, F., Krenn, E., Schulz, B., Harlov, D., & Schiller, D. (2016). "Satellite monazites" in polymetamorphic basement rocks of the Alps: Their origin and petrological significance. *American Mineralogist, 101*(5), 1094-1103. DOI: 10.2138/am-2016-5477.

Foster, G., & Parrish, R. R. (2003). Metamorphic monazite and the generation of PTt paths. *Geological Society, London, Special Publications, 220*(1), 25-47. DOI: 10.1144/GSL.SP.2003.220.01.02.

Friend, C. R. L., Kinny, P. D., Rogers, G., Strachan, R. A., & Paterson, B. A. (1997). U-Pb zircon geochronological evidence for Neoproterozoic events in the Glenfinnan Group (Moine Supergroup): the formation of the Ardgour granite gneiss, northwest Scotland. *Contributions to Mineralogy and Petrology, 128*(2-3), 101-113. DOI: 10.1007/s004100050297.

Gasser, D., & Andresen, A. (2013). Caledonian terrane amalgamation of Svalbard: detrital zircon provenance of Mesoproterozoic to Carboniferous strata from Oscar II Land, western Spitsbergen. *Geological Magazine, 150*(6), 1103-1126. DOI: 10.1017/S0016756813000174.

Gee, D. G. (1986). Svalbard's Caledonian terranes reviewed. *Geologiska Föreningen i Stockholm Förhandlingar*, *108*(3), 284-286.

Gee, D. G., & Page, L. M. (1994). Caledonian terrane assembly on Svalbard; new evidence from $^{40}Ar/^{39}Ar$ dating in Ny Friesland. *American Journal of Science, 294*(9), 1166-1186. DOI: 10.2475/ajs.294.9.1166.

Gee, D. G., & Teben'kov, A. M. (2004). Svalbard: a fragment of the Laurentian margin. *Geological Society, London, Memoirs, 30*(1), 191-206. DOI: 10.1144/GSL.MEM.2004.030.01.16.

Gee, D. G., Fossen, H., Henriksen, N., & Higgins, A. K. (2008). From the Early Paleozoic Platforms of Baltica and Laurentia to the

Caledonide Orogen of Scandinavia and Greenland. *Episodes, 31*(1), 44-51. DOI: 10.18814/epiiugs/2008/v31i1/007.

Guidotti, C. V., & Sassi F.P. (1986). Classification and correlation of metamorphic facies series by means of muscovite b(o) data from low-grade metapelites. *Neues Jahrbuch fur Mineralogie Abhandlungen, 153*, 363-380.

Hallett, B., McClelland, W., & Gilotti, J. (2014). The timing of strike-slip deformation along the Storstrømmen shear zone, Greenland Caledonides: U–Pb zircon and titanite geochronology. *Geoscience Canada, 41*(1), 19-45. DOI: 10.12789/geocanj.2014.41.038.

Harland, W. B. (1960). The Cambridge Svalbard Expedition, 1959. *Polar Record, 10*, 40-44.

Harland, W. B. (1969). *Contribution of Spitsbergen to Understanding of Tectonic Evolution of North Atlantic Region: Chapter 58: Arctic Regions*. In Kay, Marshall. North Atlantic—geology and continental drift (pp 817-851). Tulsa, Oklahoma, U.S.A.: American Association of Petroleum Geologists. DOI: 10.1306/M12367.

Harland, W. B. (1972). *Early Palaeozoic faults as margins of Arctic plates in Svalbard.* In International Geological Congress. Twenty-fourth session. Section (Vol. 3, pp. 230-237).

Harland, W. B. (1997). Proto-basement in Svalbard. *Geological Society, London, Memoirs, 17*(1), 3-15.

Harland, W. B., & Gayer, R. A. (1972). The Arctic Caledonides and earlier oceans. *Geological Magazine, 109*(4), 289-314. DOI: 10.1017/S0016756800037717.

Harland, W. B., & Wright, N. J. R. (1979). Alternative hypothesis for the pre-Carboniferous evolution of Svalbard. *Norsk Polarinstitutt Skrifter, 167*, 89-117.

Harland, W. B., Hambrey, M. J., & Waddams, P. (1993). *Vendian geology of Svalbard*. Norsk Polarinstitutt. Oslo: Skrifter.

Henry, D. J., & Guidotti, C. V. (2002). Titanium in biotite from metapelitic rocks: Temperature effects, crystal-chemical controls, and petrologic applications. *American Mineralogist, 87*(4), 375-382. DOI: 10.2138/am-2002-0401.

Higgins, A. K. (1976). Pre-Caledonian metamorphic complexes within the southern part of the East Greenland Caledonides. *Journal of the Geological Society, 132*(3), 289-305. DOI: 10.1144/gsjgs.132.3.028.

Hirajima, T., Banno, S., Hiroi, Y., & Ohta, Y. (1988). Phase petrology of eclogites and related rocks from the Motalafjella high-pressure metamorphic complex in Spitsbergen (Arctic Ocean) and its significance. *Lithos*, *22*(2), 75-97. DOI: 10.1016/0024-4937(88)90018-7.

Hjelle, A., Ohta, Y., & Winsnes, S. (1979). Hecla Hoek rocks of Oscar II Land and Prins Karls Forland, Svalbard. *Norsk Polarinstitutt Skrifter, 167*, 145-170.

Holdaway, M. J. (2001). Recalibration of the GASP geobarometer in light of recent garnet and plagioclase activity models and versions of the garnet-biotite geothermometer. *American Mineralogist, 86*(10), 1117-1129. DOI: 10.2138/am-2001-1001.

Holdsworth, R. E., & Strachan, R. A. (1991). Interlinked system of ductile strike slip and thrusting formed by Caledonian sinistral transpression in northeastern Greenland. *Geology, 19*(5), 510-513. DOI: 10.1130/0091-7613(1991)019<0510:ISODSS>2.3.CO;2.

Hollister, L. S. (1966). Garnet zoning: an interpretation based on the Rayleigh fractionation model. *Science, 154*(3757), 1647-1651. DOI: 10.1126/science.154.3757.1647.

Horsfield, W. T. (1972). Glaucophane schists of Caledonian age from Spitsbergen. *Geological Magazine, 109*(1), 29-36. DOI: 10.1017/S0016756800042242.

Janots, E., Engi, M., Berger, A., Allaz, J., Schwarz, J. O., & Spandler, C. (2008). Prograde metamorphic sequence of REE minerals in pelitic rocks of the Central Alps: implications for allanite-monazite-xenotime phase relations from 250 to 610°C. *Journal of Metamorphic Geology, 26*(5), 509-526. DOI: 10.1111/j.1525-1314.2008.00774.x.

Janots, E., Negro, F., Brunet, F., Goffé, B., Engi, M., & Bouybaouène, M. L. (2006). Evolution of the REE mineralogy in HP-LT metapelites of the Sebtide complex, Rif, Morocco: monazite stability and geochronology. *Lithos, 87*(3-4), 214-234. DOI: 10.1016/j.lithos.2005.06.008.

Johansson, Å., Gee, D. G., Björklund, L., & Witt-Nilsson, P. (1995). Isotope studies of granitoids from the Bangenhuk formation, Ny Friesland Caledonides, Svalbard. *Geological Magazine, 132*(3), 303-320. DOI: 10.1017/S0016756800013625.

Kanat, L., & Morris, A. (1988). *A working stratigraphy for central western Oscar II Land, Spitsbergen.* Oslo: Norsk Polarinstitutt. Skrifter.

Kelsey, D. E., Clark, C., & Hand, M. (2008). Thermobarometric modelling of zircon and monazite growth in melt-bearing systems: Examples using model metapelitic and metapsammitic granulites. *Journal of Metamorphic Geology*, *26*(2), 199-212. DOI: 10.1111/j.1525-1314.2007.00757.x.

Kirkland, C. L., Daly, J. S., Eide, E. A., & Whitehouse, M. J. (2006). The structure and timing of lateral escape during the Scandian Orogeny: a combined strain and geochronological investigation in Finnmark, Arctic Norwegian Caledonides. *Tectonophysics*, *425*(1-4), 159-189. DOI: 10.1016/j.tecto.2006.08.001.

Koglin, N., Läufer, A., Piepjohn, K., Gerdes, A., Davis, D. W., Linnemann, U., & Estrada, S. (2022). Palaeozoic sedimentation and Caledonian terrane architecture in northwest Svalbard: Indications from U-Pb geochronology and structural analysis. *Journal of the Geological Society, 179*(4), jgs2021-053. DOI: 10.1144/jgs2021-053.

Konečný, P., Kusiak, M.A., & Dunkley, D.J. (2018). Improving U-Th-Pb electron microprobe dating using monazite age references. *Chemical Geology 484*, 22-35. DOI: 10.1016/j.chemgeo.2018.02.014.

Konečný, P., Siman, P., Holický, I., Janák, M., & Kollárová, V. (2004). Method of monazite dating by means of the microprobe. *Mineralia Slovaca, 36*, 225-235.

Kośmińska, K., Majka, J., Mazur, S., Krumbholz, M., Klonowska, I., Manecki, M., Czerny, J., & Dwornik, M. (2014). Blueschist facies metamorphism in Nordenskiöld Land of west-central Svalbard. *Terra Nova, 26*(5), 377-386. DOI: 10.1111/ter.12110.

Kośmińska, K., Spear, F. S., Majka, J., Faehnrich, K., Manecki, M., Piepjohn, K., & Dallmann, W. K. (2020). Deciphering late Devonian-early Carboniferous P-T-t path of mylonitized garnet-mica schists from Prins Karls Forland, Svalbard. *Journal of Metamorphic Geology, 38*(5), 471-493. DOI: 10.1111/jmg.12529.

Kośmińska, K., Gilotti, J. A., McClelland, W. C., Coble, M. A., & Thomas, J. B. (2022). P–T–t path of unusual garnet–kyanite–staurolite–amphibole schists, Ellesmere Island, Canada—Quartz inclusion in garnet barometry and monazite petrochronology. *Journal of Petrology*, *63*(8), egac068. DOI: 10.1093/petrology/egac068.

Krasil'ščikov, A. A., Kubanskij, A. P., & Ohta, Y. (1995). Surface magnetic anomaly study on the eastern part of the Forlandsundet Graben. *Polar Research*, *14*(1), 55-68. DOI: 10.3402/polar.v14i1.6651.

Krenn, E., & Finger, F. (2007). Formation of monazite and rhabdophane at the expense of allanite during Alpine low temperature retrogression of metapelitic basement rocks from Crete, Greece: Microprobe data and geochronological implications. *Lithos, 95*(1-2), 130-147. DOI: 10.1016/j.lithos.2006.07.007.

Krenn, E., Ustaszewski, K., & Finger, F. (2008). Detrital and newly formed metamorphic monazite in amphibolite-facies metapelites from the Motajica Massif, Bosnia. *Chemical Geology*, *254*(3-4), 164-174. DOI: 10.1016/j.chemgeo.2008.03.012.

Labrousse, L., Elvevold, S., Lepvrier, C., & Agard, P. (2008). Structural analysis of high-pressure metamorphic rocks of Svalbard: Reconstructing the early stages of the Caledonian orogeny. *Tectonics, 27*(5). DOI: 10.1029/2007TC002249.

Lanari, P., Vho, A., Bovay, T., Airaghi, L., & Centrella S. (2019). Quantitative compositional mapping of mineral phases by electron probe micro-analyser. *Geological Society of London, Special Publications, 478*(1), 39-63. DOI: 10.1144/SP478.4.

Lanari, P., Vidal, O., De Andrade, V., Dubacq, B., Lewin, E., Grosch, E. G., & Schwartz, S. (2014*).* XMapTools: A MATLAB©-based program for electron microprobe X-ray image processing and geothermobarometry. *Computers and Geosciences, 62*, 227-240. DOI: 10.1016/j.cageo.2013.08.010.

Lyberis, N., & Manby, G. (1999). Continental collision and lateral escape deformation in the lower and upper crust: an example from Caledonide Svalbard. *Tectonics, 18*(1), 40-63. DOI: 10.1029/1998TC900013.

Maher Jr, H. D., Bergh, S., Braathen, A., & Ohta, Y. (1997). Svartfjella, Eidembukta, and Daudmannsodden lineament: Tertiary orogen-parallel motion in the crystalline hinterland of Spitsbergen's fold-thrust belt. *Tectonics, 16*(1), 88-106. DOI: 10.1029/96TC02616.

Majka, J., & Kośmińska, K. (2017). Magmatic and metamorphic events recorded within the Southwestern Basement Province of Svalbard. *Arktos, 3*(1), 1-7. DOI: 10.1007/s41063-017-0034-7.

Majka, J., Be'eri-Shlevin, Y., Gee, D., Czerny, J., Frei, D., & Ladenberger, A. (2014). Torellian (c. 640 Ma) metamorphic overprint of Tonian (c. 950 Ma) basement in the Caledonides of southwestern Svalbard. *Geological Magazine, 151*(4), 732-748. DOI: 10.1017/S0016756813000794.

Majka, J., Kośmińska, K., Mazur, S., Czerny, J., Piepjohn, K., Dwornik, M., & Manecki, M. (2015). Two garnet growth events in polymetamorphic rocks in southwest Spitsbergen, Norway: insight in the history of Neoproterozoic and early Paleozoic metamorphism in the High Arctic. *Canadian Journal of Earth Sciences, 52*(12), 1045-1061. DOI: 10.1139/cjes-2015-0142.

Majka, J., Mazur, S., Manecki, M., Czerny, J., & Holm, D. K. (2008). Late Neoproterozoic amphibolite-facies metamorphism of a pre-Caledonian basement block in southwest Wedel Jarlsberg Land, Spitsbergen: New evidence from U-Th-Pb dating of monazite. *Geological Magazine, 145*(6), 822-830. DOI: 10.1017/S001675680800530X.

Manby, G. (2014). Deciphering the tectonic evolution of the Prins Karls Forland-Oscar II Land Caledonide domain of Svalbard. In W. K. Dallmann, M. Manecki, K. Michalski, & P. Głowacki (Eds). *SVALGEOBASE: Proterozoic and Lower Palaeozoic basement of Svalbard-state of knowledge and new perspectives of investigations.* Workshop report (p. 23). Tromsø, Norway: Norsk Polarinstitutt.

Manby, G. M. (1986). Mid-Palaeozoic metamorphism and polyphase deformation of the Forland Complex, Svalbard. *Geological Magazine, 123*(6), 651-663. DOI: 10.1017/S001675680002416X.

Mazur, S., Czerny, J., Majka, J., Manecki, M., Holm, D., Smyrak, A., & Wypych, A. (2009). A strike-slip terrane boundary in Wedel Jarlsberg Land, Svalbard, and its bearing on correlations of SW Spitsbergen with the Pearya terrane and Timanide belt. *Journal of the Geological Society, 166*(3), 529-544. DOI: 10.1144/0016-76492008-106.

McCann, A. J. (2000). Deformation of the Old Red Sandstone of NW Spitsbergen; links to the Ellesmerian and Caledonian orogenies. *Geological Society, London, Special Publications, 180*(1), 567-584. DOI: 10.1144/GSL.SP.2000.180.01.30.

McClelland, W. C., Malone, S. J., von Gosen, W., Piepjohn, K., & Läufer, A. (2012). The timing of sinistral displacement of the Pearya Terrane along the Canadian Arctic Margin. *Zeitschrift der deutschen Gesellschaft fuer Geowissenschaften, 163*(3), 251-259. DOI: 10.1127/1860-1804/2012/0163-0251.

McClelland, W. C., Strauss, J. V., Colpron, M., Gilotti, J. A., Faehnrich, K., Malone, S. J., Gehrels, G. E., Macdonald, F. A., & Oldow, J. S. (2021). Taters versus Sliders: Evidence for a Long-Lived History of Strike-Slip Displacement along the Canadian Arctic Transform System (CATS). *GSA Today, 31*(7), 4–11. DOI: 10.1130/GSATG500A.1.

Michalski, K., Domańska-Siuda, J., Nejbert, K., & Manby, G. (2014). New palaeomagnetic data from metamorphosed carbonates of Western Oscar II Land, Western Spitsbergen. *Polish Polar Research, 4,* 553-592. DOI: 10.24425/118738.

Michalski, K., Lewandowski, M., & Manby, G. (2012). New palaeomagnetic, petrographic and $^{40}Ar/^{39}Ar$ data to test palaeogeographic reconstructions of Caledonide Svalbard. *Geological Magazine, 149*(4), 696-721. DOI: 10.1017/S0016756811000835.

Montel, J. M., Foret, S., Veschambre, M., Nicollet, C., & Provost, A. (1996). Electron microprobe dating of monazite. *Chemical Geology, 131*(1-4), 37-53. DOI: 10.1016/0009-2541(96)00024-1.

Morris, A. (1988). Polyphase deformation in Oscar II Land, central western Svalbard. *Polar Research, 6*(1), 69-84. DOI: 10.3402/polar.v6i1.6847.

Mulch, A., & Cosca, M. A. (2004). Recrystallization or cooling ages: in situ UV-laser $^{40}Ar/^{39}Ar$ geochronology of muscovite in mylonitic rocks. *Journal of the Geological Society, 161*(4), 573-582. DOI: 10.1144/0016-764903-110.

Ohta, Y. (1979). Blueschists from Motalafjella, western Spitsbergen. *Norsk Polarinstitutt Skrifter, 167*, 171-217.

Ohta, Y. (1985). Geochemistry of Precambrian basic igneous rocks between St. Jonsfjorden and Isfjorden, central western Spitsbergen, Svalbard. *Polar Research, 3*(1), 49-67. DOI: 10.1111/j.1751-8369.1985.tb00494.x.

Ohta, Y. (1994). Caledonian and Precambrian history in Svalbard: a review, and an implication of escape tectonics. *Tectonophysics, 231*(1-3), 183-194. DOI: 10.1016/0040-1951(94)90129-5.

Ohta, Y., Dallmeyer, R. D., & Peucat, J. J. (1989). Caledonian terranes in Svalbard. In R.D. Dallmeyer (Ed.), *Terranes in the Circum-Atlantic Paleozoic Orogens* (1-15). Boulder, CO, United States: *Geological Society of America.* DOI: 10.1130/SPE230-p1.

Ohta, Y., Hiroi, Y., & Hirajima, T. (1983). Additional evidence of pre-Silurian high-pressure metamorphic rocks in Spitsbergen. *Polar Research, 1*(2), 215-218. DOI: 10.3402/polar.v1i2.6986.

Ohta, Y., Krasil'šikov, A. A., Lepvrier, C., & Teben'kov, A. M. (1995). Northern continuation of Caledonian high-pressure metamorphic rocks in central-western Spitsbergen. *Polar Research*, *14*(3), 303-316. DOI: 10.3402/polar.v14i3.6670.

Palin, R. M., Searle, M. P., St-Onge, M. R., Waters, D. J., Roberts, N. M. W., Horstwood, M. S. A., Parish, R. R., & Weller, O. M. (2015). Two-stage cooling history of pelitic and semi-pelitic mylonite (sensu lato) from the Dongjiu-Milin shear zone, northwest flank of the eastern Himalayan syntaxis. *Gondwana Research, 28*(2), 509-530. DOI: 10.1016/j.gr.2014.07.009.

Pan, Y. (1997). Zircon-and monazite-forming metamorphic reactions at Manitouwadge, Ontario. *The Canadian Mineralogist, 35*(1), 105-118.

Petrík, I., & Konečný, P. (2009). Metasomatic replacement of inherited metamorphic monazite in a biotite-garnet granite from the Nízke Tatry Mountains, Western Carpathians, Slovakia: Chemical dating and evidence for disequilibrium melting. *American Mineralogist, 94*(7), 957-974. DOI: 10.2138/am.2009.2992.

Piepjohn, K., & Thiedig, F. (1995). Tektonische Entwicklung des kristallinen Basements im Liefdefjorden-Gebiet, NW-Svalbard. (Tectonic development of crystalline basements in the Liefdefjorden area, north-west Spitsbergen.) *Münstersche Forschungen zur Geologie und Paläontologie, 77*, 1-25.

Piepjohn, K., Griem-Klee, S., Post, H., Post, J., & Thiedig, F. (2000). Geology and structural evolution of pre-Caledonian rocks and the? Devonian Sutorfjella conglomerate, northern Prins Karls Forland (Svalbard). *Norsk Geologisk Tidsskrift, 80*(2), 83-95. DOI: 10.1080/002919600750042582.

Piepjohn, K., von Gosen, W., & Tessensohn, F. (2016). The Eurekan deformation in the Arctic: an outline. *Journal of the Geological Society, 173*(6), 1007-1024. DOI: 10.1144/jgs2016-081.

Ratliff, R., Morris, A., & Dodt, M. (1988). Interaction between strike-slip and thrust-shear: deformation of the Bullbreen Group, central-western Spitsbergen. *The Journal of Geology, 96*(3), 339-349. DOI: 10.1086/629224.

Savko, K. A., & Bazikov, N. S. (2011). Phase equilibria of bastnaesite, allanite, and monazite: Bastnaesite-out isograde in metapelites of the Vorontsovskaya group, Voronezh crystalline massif. *Petrology, 19*(5), 445-469. DOI: 10.1134/S0869591111030076.

Scrutton, C. T., Horsfield, W. T., & Harland, W. B. (1976). Silurian fossils from western Spitsbergen. *Geological Magazine, 113*(6), 519-523. DOI: 10.1017/S0016756800041261.

Seydoux-Guillaume, A. M., Deschanels, X., Baumier, C., Neumeier, S., Weber, W. J., & Peuget, S. (2018). Why natural monazite never becomes amorphous: Experimental evidence for alpha self-healing. *American Mineralogist, 103*(5), 824-827. DOI: 10.2138/am-2018-6447.

Spear, F. S. (2010). Monazite-allanite phase relations in metapelites. *Chemical Geology, 279*(1-2), 55-62. DOI: 10.1016/j.chemgeo.2010.10.004.

Tessensohn, F., von Gosen, W., & Piepjohn, K. (2001). Permo-Carboniferous slivers infolded in the basement of Western Oscar II Land. *Geologisches Jahrbuch Reihe B91*, 161-204.

Tracy, R. J., Robinson, P., & Thompson, A. B. (1976). Garnet composition and zoning in the determination of temperature and pressure of metamorphism, central Massachusetts. *American Mineralogist, 61*(7-8), 762-775.

Trettin, H. P. (1987). Pearya: a composite terrane with Caledonian affinities in northern Ellesmere Island. *Canadian Journal of Earth Sciences, 24*(2), 224-245. DOI: 10.1139/e87-025.

Trettin, H. P. (1998). Geology of Pearya, in Pre-Carboniferous geology of the northern part of the Arctic Islands: Northern Heiberg Fold Belt, Clements Markham Fold Belt, and Pearya; northern Axel Heiberg and Ellesmere islands. *Geological Survey of Canada Bulletin, 425*, 108-192.

Tursi, F. (2022). The key role of μH_2O gradients in deciphering microstructures and mineral assemblages of mylonites: Examples from the Calabria polymetamorphic terrane. *Mineralogy and Petrology*, *116*(1), 1-14. DOI: 10.1007/s00710-021-00766-8.

Tyrell, G. W. (1924). The geology of Prince Charles' Foreland, Spitsbergen. *Royal Geological Society of Edinburgh Transactions, 53*, 443-478.

von Gosen, W., Piepjohn, K., McClelland, W. C., & Läufer, A. (2012). The Pearya shear zone in the Canadian High Arctic: Kinematics and significance. *Zeitschrift der Deutschen Gesellschaft für Geowissenschaften, 163*(3), 233-249. DOI: 10.1127/1860-1804/2012/0163-0233.

Wala, V. T., Ziemniak, G., Majka, J., Faehnrich, K., McClelland, W. C., Meyer, E. E., Manecki, M., Bazarnik. J., & Strauss, J. V. (2021). Neoproterozoic stratigraphy of the Southwestern Basement Province, Svalbard (Norway): Constraints on the Proterozoic-Paleozoic evolution of the North Atlantic-Arctic Caledonides. *Precambrian Research*, *358*, 106138. DOI: 10.1016/j.precamres.2021.106138.

Whitney, D. L., & Evans, B. W. (2010). Abbreviations for names of rock-forming minerals. *American Mineralogist, 95*(1), 185-187. DOI: 10.2138/am.2010.3371.

Wing, B. A., Ferry, J. M., & Harrison, T. M. (2003). Prograde destruction and formation of monazite and allanite during contact and regional metamorphism of pelites: petrology and geochronology. *Contributions to Mineralogy and Petrology, 145*(2), 228-250. DOI: 10.1007/s00410-003-0446-1.

Wu, C. M. (2019). Original calibration of a garnet geobarometer in metapelite. *Minerals, 9*(9), 540. DOI: 10.3390/min9090540.

Yang, P., & Pattison, D. (2006). Genesis of monazite and Y zoning in garnet from the Black Hills, South Dakota. *Lithos, 88*(1-4), 233-253. DOI: 10.1016/j.lithos.2005.08.012.

Received: 04 Jun 2022
Accepted: 05 Dec 2022
Handling Editor: Silvio Ferrero